SMPD3-mediated extracellular vesicle biogenesis inhibits oligodendroglioma growth

Abbreviated Title: Vesicular control of oligodendroglioma growth

Anjali Balakrishnan[1,2], Lata Adnani[1,3*], Vorapin Chinchalongporn[1], Lakshmy Vasan[1,4], Oleksandr Prokopchuk[1], Myra J Chen[5], Ahmed El-Sehemy[4,6], Thomas Olender[7], Yacine Touahri[1], Shiekh Tanveer Ahmad[5,8ψ], Rehnuma Islam[9], Sajeevan Sujanthan[1], Dawn Zinyk[1], Lacrimioara C Comanita[6], Boris Kan[1], Taylor Fleming[1], Hon S Leong[1], Cindi M Morshead[9], Marjorie Brand[7], Valerie A Wallace[4,6,10], Jennifer A Chan[3*], Carol Schuurmans[1,2,3,4*]

Affiliations :

[1] Sunnybrook Research Institute, Toronto, ON, Canada
[2] Department of Biochemistry, University of Toronto, Toronto, ON, Canada
[3] Department of Biochemistry and Molecular Biology, Alberta Children's Hospital Research Institute, Hotchkiss Brain Institute, University of Calgary, Calgary, AB, Canada
[4] Department of Laboratory Medicine and Pathobiology, University of Toronto, Toronto, ON, Canada
[5] Department of Pathology and Laboratory Medicine, Charbonneau Cancer Institute, Alberta Children's Hospital Research Institute, University of Calgary, Calgary, AB, Canada
[6] Donald K. Johnson Eye Institute, Krembil Research Institute, University Health Network
[7] Ottawa Hospital Research Institute, Ottawa, Ontario, Canada
[8] Department of Developmental Neurobiology, St Jude Children's Research Hospital, Memphis, TN, USA
[9] Department of Surgery, University of Toronto, Toronto, ON, Canada
[10] Department of Ophthalmology and Vision Sciences, University of Toronto, Toronto, ON, Canada

Corresponding author: Carol Schuurmans (cschuurm@sri.utoronto.ca)
Biological Sciences Platform, Sunnybrook Research Institute, Room S116A, 2075 Bayview Avenue, Toronto, ON M4N 3M5, Canada

*co-senior authors

Keywords: IDH mutation, lower grade glioma, oligodendroglioma, extracellular vesicles, *SMPD3*, nSMase2, tumor xenograft, cerebral organoid

[#] Current address: The Research Institute of the McGill University Health Centre, Montreal, QC, Canada.

[ψ] Current address: Department of Developmental Neurobiology, St Jude Children's Research Hospital, Memphis, TN, USA

ABSTRACT
Oligodendrogliomas are lower-grade, slow-growing gliomas that are ultimately fatal. Although driver mutations are known, the mechanisms underlying their signature slow growth rates are poorly understood. We found evidence for intra-tumoral interactions between neoplastic and non-neoplastic cells in oligodendroglioma tissues. To further study these cell interactions, we used two patient-derived oligodendroglioma cell lines of lower and higher aggressivity. Both oligodendroglioma cell lines released extracellular vesicles that had cytotoxic effects on non-neoplastic and neoplastic cells, but each had distinct vesicular proteomes. Consistent with extracellular vesicles mediating growth inhibitory effects in oligodendrogliomas, higher expression levels of several extracellular vesicle biogenesis genes (*SMPD3,TSG101, STAM1)* correlates with longer survival in oligodendroglioma patients. Furthermore, *SMPD3* overexpression slows oligodendroglioma cell growth in culture. Conversely, *SMPD3* knockdown enhances oligodendroglioma proliferation *in vitro*, in murine xenografts, and in human cerebral organoid co-cultures. Oligodendroglioma-derived extracellular vesicles thus mediate tumor cell microenvironmental interactions that contribute to low aggressivity.

INTRODUCTION

Gliomas are a heterogenous group of primary glial brain tumors that are composed of a mixture of neoplastic glial cells ('tumor cells') and non-neoplastic 'stromal cells' that include non-neoplastic glia, neurons, and a variety of other inflammatory and vascular cells[1, 2]. Gliomas are classified based on their molecular and histological features[3, 4]. The most aggressive and most frequently studied is glioblastoma multiforme (GBM), a high-grade astrocytoma with 5-year survival rates of less than 5%[5]. In contrast, lower-grade gliomas (World Health Organization–WHO stage II/III tumors), which include oligodendroglioma (ODG), are slower growing tumors, with median survival times between 9-14 years[6]. Glioma subtypes each have a unique constellation of mutations, that in ODG typically includes isocitrate dehydrogenase 1 (IDH1) or IDH2 mutations, chromosomal 1p/19q co-deletion, and mutation of Capicua (CIC), a transcriptional repressor, in the retained 19q allele [7, 8, 9, 10]. While tumor cells carry driver mutations that are responsible for the cells neoplastic transformation, non-neoplastic cells in the tumor microenvironment form part of the ecosystem that sustains tumor cell proliferation and growth[11]. Understanding how glioma cells interact with cells in the microenvironment is thus essential to understanding disease progression.

Extracellular vesicles (EVs) are important mediators of intercellular communication. EVs package lipids, protein, DNA and RNA in a lipid bilayer that protects cargo from degradation in the extracellular space and facilitates membrane fusion and delivery of bioactive material to neighboring cells[12]. Small EVs (sEVs; 40-200nm), also known as exosomes, are generated via different biogenic enzymes, including endosomal sorting complex related transport (ESCRT)-dependent and -independent pathways[12]. ESCRT-independent biogenesis is mediated by s*phingomyelin phosphodiesterase 3 (SMPD3)*, encoding neutral sphingomyelinase 2 (nSMase2), which produces ceramide required for exosome generation and budding[13]. EVs are secreted by most if not all cells in the brain, including oligodendrocytes[14], astrocytes[15], neurons[16], as well as cancerous cells[17]. There are now several examples of glioma cells interacting with cells in the tumor niche via EVs[18, 19]. Strikingly, while EVs from higher-grade gliomas are generally growth promoting, the few studies conducted with ODG suggest that ODG-derived EVs may be cytotoxic[20, 21].

Here, we further queried how vesicular factors contribute to the slow growth properties of ODG, using patient using patient tissue samples, patient-derived ODG cell lines[9], and publicly available molecular and clinical glioma data. We found evidence that ODG cells exert growth inhibitory effects non-cell autonomously in part through the secretion of cytotoxic vesicular factors. Accordingly, higher expression levels of several EV biogenic genes (*SMPD3, TSG101, STAM1*) correlates positively with longer survival in low-grade glioma patients. We focused on *SMPD3* and found that it is a critical regulator of cytotoxic EV biogenesis in ODG. *SMPD3* negatively regulates ODG growth in cultured cells, in mouse xenografts, and in human cerebral organoid co-cultures. We conclude that ODG cells negatively modulate tumor growth in part through the secretion of vesicular factors that have homotypic and heterotypic cytotoxic effects on cells in the tumor niche.

RESULTS

Oligodendroglioma cells exert non-cell autonomous effects within the tumor niche

To determine whether lower-grade glioma cells interact non-cell autonomously with neighboring non-neoplastic cells (heterotypic interactions) in the tumor microenvironment, we analyzed surgical resection specimens from five IDH-mutant, 1p/19q-codeleted ODG patients

(Table 1). We imaged tumor sections in the more confluent tumor core and in peritumoral infiltrating regions, where we reasoned that tumor cells could influence non-neoplastic reactive cells. To identify tumor cells, sections were immunolabeled with an antibody to IDHmR132H (hereafter IDHm)[22]. As expected, co-staining with IDHm and OLIG2, an oligodendrocyte lineage marker highly expressed in ODG[23], showed high co-localization of IDHm and OLIG2 in all samples (Fig. 1A-E).

We then asked whether IDHm-negative non-neoplastic cells in the core and peritumoral regions were influenced by the tumor by assessing proliferation, a rare event in non-cancerous adult brains[24]. Co-labeling with IDHm and Ki-67, a pan-proliferative marker, showed that a surprisingly large fraction of Ki-67$^+$ cells (83-88%) were IDHm-negative (Fig. 1F-J). Proliferation of non-neoplastic cells in the tumor mass suggested that tumor cells could secrete growth factors or other signals that modulate the behavior of neighboring cells. Consistent with the presence of non-cell autonomous signaling in the microenvironment, we detected MEK/ERK pathway activation (as evidenced by pERK staining) in IDHm-negative cells (Fig. S1A-E, Table S1).

Although correlative in nature, these findings are consistent with the idea that IDH mutant ODG cells may communicate with neighboring stromal cells (neural, vascular, inflammatory) in the tumor niche in a non-cell autonomous fashion (Fig. 1K).

ODG secretomes have distinct bioactive effects but both include cytotoxic EVs

To mediate contact-independent communication, tumor cells and neighboring non-neoplastic stromal cells secrete a variety of bioactive molecules (e.g. growth factors, cytokines, interleukins) that are enriched in the tumor microenvironment[25]. *In vitro*, bioactive factors are found in tumor conditioned media (CM), as soluble factors and/or in EVs[12]. To further understand how ODG cells interact with cells in the tumor microenvironment, we used two different patient-derived cell lines established from IDH-mutant, 1p/19q co-deleted anaplastic ODGs, termed BT088 and BT054 cells[9]. Both cell lines can self-renew and grow *in vitro*, but only BT088 cells, isolated from a higher grade III tumor, retain the ability to form tumors after xenografting in immunocompromised mice[9]. Consistent with reported differences in tumor growth *in vivo*, using real-time live cell imaging, we found that BT088 cells have a 1.76-fold shorter doubling time than BT054 cells when grown *in vitro* (Fig. 2A, Table S1).

To ask whether BT088 and BT054 ODG cells might influence the growth/survival of neighboring cells in the tumor niche, we tested the bioactivity of secreted factors on two cell types - embryonic neural stem cells (eNSCs) and ODG cells themselves (Fig. 2B). While eNSCs are not present in the adult tumor niche, they were chosen as a surrogate cell type as their growth is highly sensitive to external cues[26]. Embryonic day (E) 12.5 NSCs isolated from the cortex were first plated at clonal density in fresh media (FM), or CM collected from the two ODG cell lines. After 7 days *in vitro* (DIV), neurosphere number (measure of activated NSCs), neurosphere size (aggregate measure of proliferation and apoptosis) and live cell number (measure of cell survival) were quantitated (Fig. 2C-F). Compared to FM, NSCs grown in BT088-CM gave rise to more neurospheres that were larger in size (Fig. 2C-I, all counts in Table S1). However, the larger spheres had markedly fewer live cells (Fig. 2J, Table S1). In contrast, BT054 CM did not alter neurosphere number, and it had an inhibitory effect on both neurosphere size and live cell number compared to FM (Fig. 2K-N). Thus, while BT088 CM initially promotes NSC revival from quiescence and NSC proliferation, cell progeny have decreased viability. In contrast, BT054 CM in aggregate is not pro-proliferative, but like BT088 cells, BT054 cells also secrete cytotoxic factors.

The bioactive effects of ODG CM could be due to soluble and/or EV-enclosed factors. To dissect this activity further, we repeated the neurosphere assay using CM in which EVs were removed by sequential centrifugation (CM-EV). E12.5 NSCs grown in BT088 CM-EV formed the same number of neurospheres as NSCs grown in BT088 CM, however, there was a further increase in neurosphere size, and a striking increase in live cell number (Fig. 2C-J; Table S1). Similarly, E12.5 NSCs grown in BT054 CM-EV formed the same number of neurospheres as NSCs grown in BT054 CM, and there was an increase in neurosphere size, although live cell number was not altered (Fig. 2K-N; Table S1). Thus, BT088 CM contains pro-proliferative factors that are largely soluble, and cytotoxic factors that are mainly vesicular. In contrast, BT054 CM contains soluble pro-proliferative factors, the activity of which is masked by cytotoxic factors that are both soluble and vesicular.

Next, to directly assess EV bioactivity, EVs were added to FM (FM+EV). BT088 EVs added to FM reduced neurosphere number, neurosphere size and live cell number compared to FM (Fig. 2C-J, Table S1). In contrast, BT054 EVs added to FM did not alter neurosphere number, while neurosphere size and live cell number were both reduced compared to FM (Fig. 2K-N, Table S1). Thus, BT088 and BT054 cells both produce EVs that carry cytotoxic factors.

Finally, to determine whether the cytotoxic nature of BT088 EVs translated to other cell types, we directly examined BT088 EV effects on BT088 cell growth (i.e. homotypic activity) using a similar tumorsphere assay (Fig. 2B). Notably, BT088 EVs had a similar cytotoxic effect on BT088 cells themselves, reducing tumorsphere size and live cell number after 5 DIV (Fig. 2O-S), suggesting that ODG cells may limit their own growth/survival by EV-mediated autocrine/paracrine effects.

Taken together, these studies confirm that while ODG CM from both BT088 and BT054 cell lines contains pro-proliferative soluble factors, in addition to EV-enclosed factors that induce cell death, which in BT054 cells, overshadows the pro-proliferative effects. These differences in the bioactive nature of the BT054 and BT088 secretomes may help to explain their different growth rates (Fig. 2A) and tumorigenicity[9].

ODG EVs induce proliferation followed by apoptosis

The ability of BT088 CM to induce the formation of more and larger neurospheres suggested that pro-proliferative effects could occur first, followed by cell death. To interrogate the timeline of events, we performed live cell imaging using phase area confluence as a surrogate measure of cell number (Fig. 2T). NSCs plated in either BT088 CM or CM-EVs increased in number after 5 DIV at a faster rate than NSCs grown in FM or FM+EV (Fig. 2U). However, after 5 DIV, while NSCs continued to grow exponentially in CM-EV, cell number started to decline in CM (Fig. 2U). There was also a decrease in cell number in FM+EV compared to FM, which supports the notion that EVs carry cytotoxic factors (Fig. 2U).

We further confirmed the cytotoxic nature of BT088 EVs by performing live cell imaging after incorporating a fluorescent cytotoxic dye ('Cytotox') into NSC cultures. A decline in cellular health increases cell permeability thereby permitting entry and intercalation of Cytotox into affected cells. After 3 DIV, NSCs exposed to CM and FM+EVs incorporated Cytotox at a higher rate than cells grown in FM or CM-EV, validating the cytotoxic nature of the EVs (Fig. 2V; Fig S1F-Q). Finally, to determine whether BT088 EVs exerted a pro-apoptotic effect on NSCs, AnnexinV/Propidium Iodide (PI) co-labeling of late apoptotic cells was assessed via flow cytometry[27] (Fig. S1R). After 3 DIV, NSCs grown in FM included 3.8% AnnexinV$^+$PI$^+$ late apoptotic cells, whereas nearly 52.7% of NSCs grown in FM+EV were double$^+$ apoptotic cells

(Fig. S1S). Similarly, NSCs cultured for 3 DIV in BT088 CM included 55.6% AnnexinV$^+$PI$^+$ late apoptotic cells, and this number declined to 35% when grown in CM-EV (Fig. S1S).

In summary, BT088 CM has an initial pro-proliferative effect that is followed a few days later by an increase in EV-mediated cell death, suggesting that ODG EVs induce apoptosis of NSC progeny.

ODG cells secrete bioactive EVs mainly in the 40-200 nm exosome size range

To determine whether the isolated 'EVs' tested above were truly vesicular, we characterized their morphology and protein content. First, we used scanning electron microscopy to assess cellular topography, revealing the presence of budding vesicles on the surfaces of both BT054 and BT088 cells (Fig. 3A,B). Next, to assess vesicular size and composition, EVs were isolated from CM using sequential centrifugation[12]. Using transmission electron microscopy, we demonstrated that sedimented particles isolated from ODG cells had a lipid bilayer-enclosed nanoparticle morphology characteristic of EVs (BT088 EVs shown, Fig. 3C,C'). To calculate the size and number of isolated EVs, we used nanosight tracking analysis (NTA). BT054 and BT088 cells both produced EVs that were largely within the exosome size range (i.e. 40-200 nm [28], Fig. 3D,E, Table S1), but BT088 cells produced twice as many EV particles (Table S1). Finally, as a first assessment of molecular phenotype of ODG EVs, using nanoscale-flow cytometry we revealed that 13.7±2.0% of BT088 EVs expressed CD9, a marker of a subset of EVs[29] (Fig. 3G).

To further assess the molecular nature of ODG EVs, we focused on BT088 EVs, as they were more numerous. Using Western blotting, we compared protein content in the crude cell lysate (CL) and in the EV pellet. Compared to CL, EVs were enriched in EV-associated markers[30], including Alix, CD9 and Cetp (Fig. 3H). Flotillin1, a common EV marker, was also detected in EVs, but was also present at high levels in CL due to its association with the cell membrane[31] (Fig. 3H). Finally, we confirmed the relative purity of the EV preparations by probing for proteins associated with other organelles, including the endoplasmic reticulum (Calreticulin, Calnexin), mitochondria (Vdac), Golgi bodies (GM130) and peroxisomes (Pex5), all of which were detected in the CL, as expected, and at negligible levels in EVs (Fig. 3I).

As the sequential centrifugation method of EV isolation is sedimentation-based, it can also isolate non-vesicular components[28]. To determine whether non-vesicular material was in the 'EV' pellet, we used density gradient ultracentrifugation for size fractionation. BT088-EVs isolated by sequential ultracentrifugation were loaded onto a discontinuous Optiprep™ gradient. After ultracentrifugation, eight fractions were collected from the density gradient, and analyzed by Western blotting and NTA. EV associated markers (Alix, CD9, Cetp) were detected in fractions 4 and 5, with a density of 1.08-1.09 g/cm^3, while negative EV markers (Vdac, Calnexin) were absent in these fractions (Fig. 3J). Using NTA, we confirmed that EV particles in layer 4 were predominantly in the exosome size range (Fig. 3F). Of note, Cetp was also detected in low density fractions 1-3 (0.95-1.07 g/cm^3), which contain non-vesicular low-density lipoproteins to which Cetp associates[32]. Thus, the BT088-EV pellet collected by ultracentrifugation includes EVs mainly in the exosome size range but also some microvesicles and non-vesicular material, as previously shown for other cell types[28].

EVs deliver molecular content to neighboring cells through membrane fusion, a delivery method not available to non-vesicular material. To determine whether BT088 cells secrete bioactive cargo in EVs that can be taken up by and influence recipient cells, we used a Cre recombinase-based fluorescent reporter assay previously used to report EV-mediated Cre transfer[33]. BT088 'donor' cells were stably transduced to express Cre recombinase and GFP, while

NIH-3T3 'recipient' cells were transduced with a dual BFP-dsRed Cre reporter[33]. BFP is expressed in recipient cells prior to Cre (mRNA/protein) transfer from donor-to-recipient cells, which undergo Cre mediated excision of a STOP cassette to then allow expression of dsRed. We aggregated BT088-GFP-Cre donor cells with NIH-3T3 BFP-dsRed recipient cells (Fig. 3K). After 3 DIV, we detected RFP^+ cells that were GFP^-, indicating that they did not arise from cell fusion (Fig. 3L-O).

BT088 cells thus secrete bioactive cargo to recipient cells, and from our *in vitro* assays, we suggest that this includes EVs and other soluble factors.

Proteomic profiling reveals ODG cells secrete distinct vesicular cargo

To characterize the potential bioactive content of ODG EVs, we carried out proteomic analyses of BT088 and BT054 vesiculomes by LC-MS/MS (Fig. 4A). Given the known differences in biologic behavior of the two cell lines, it was unsurprising that the protein content differed between the two EV pools, with 390 proteins detected in BT088 EVs and 186 proteins in BT054 EVs, of which only 72 proteins were common between the two vesiculomes (minimum 2 out of 3 individual replicates; Fig. 4A'). Among the shared proteins, both BT088 and BT054 EVs contained commonly associated EV proteins (e.g. Alix, CD63; Table S3[28, 34]), validating the vesicular nature of our preparations.

BT088 and BT054 vesiculomes were enriched in proteins associated with several biological processes, including metabolic, developmental, immune system, growth and cell death (Fig. 4B). In both BT088 and BT054 vesiculomes, several identified proteins were assigned to cell death pathways, some of which were higher in BT088 EVs (e.g. RHOA, RPL11; Fig. 4C,D), others elevated in the BT054 vesiculome (e.g. HTRA1 (Fig. 4E), and some common to EVs from both cell types (e.g. CLU; Fig. 4F). Notably, of the proteins associated with proliferation, such as PKM, HSPB1, HSP90AA1, and HSP90AB1 (Fig. 4G-J), all were detected at higher levels in the BT088 versus BT054 vesiculome, in keeping with differences in the growth rates of these two tumor cell lines[9].

While our data suggested that cytotoxic signals largely overshadow pro-proliferative signals in ODG-derived EVs, BT088 and BT054 tumor cells continue to grow and thrive. To understand how ODG cell proliferation is supported, we queried the proteome for growth regulators, as proteins are loaded into EVs non-specifically, and serve as an informative readout of cellular state[28]. Two proteins detected in both BT088 and BT054 EVs stood out - SRI (Sorcin) and MFGE8 (Lactadherin) (Fig. 4K,L). SRI expression is elevated in several cancers, including breast, hepatocellular, and gastric[35], and it is required to maintain VEGF expression, which is involved in angiogenesis, tumor invasion, and metastasis[35, 36]. Similarly, MFGE8 promotes VEGF-dependent neovascularization in endothelial cells[37]. In line with the viewpoint that EVs are non-specific carriers of cellular protein, and that EV content implies signaling status [28], we inferred that VEGF signaling may be activated in these two ODG cell lines. To assess the importance of VEGF signaling in supporting ODG tumor growth, we treated BT088 cells with Foretinib, a VEGF-receptor inhibitor[38], at five different concentrations (50 nM-500 nM) and cell growth was assessed over five days using live cell imaging. Strikingly, in all conditions, BT088 cell growth resembled BT054 growth (Fig. 2A), with increase in BT088-cell doubling times (from 4-9 fold) at all concentrations, compared to BT088 cells grown in DMSO (Fig. 4M). Foretinib treatment of BT088 cells also increased cytotoxicity at all assessed doses and inhibited growth of BT088 cells (Fig. 4N).

BT088 and BT054 vesiculomes are thus distinct from each other, revealing the heterogeneity of ODG intracellular signaling and the potential pathways that may trigger cell death in neighboring cells.

Lower *SMPD3* expression is associated with poor prognosis in oligodendroglioma patients

Given that BT088 and BT054 EVs both had cytotoxic effects, we queried whether EV generation was itself associated with ODG biologic behavior. We analyzed data from the cancer genome atlas (TCGA) database to compare expression of genes involved in ESCRT-dependent (*TSG101, STAM1*) [12], and ESCRT-independent (*SMPD3*)[13] exosome synthesis in a lower grade glioma patient cohort, correlating gene expression with patient survival. Strikingly, lower *TSG101, STAM1,* and *SMPD3* expression levels correlated with shorter survival times compared to patients with higher expression of these genes (Fig. 5A-C; $p<0.0001$, Table S1), consistent with the notion that exosome synthesis may play a role in limiting lower grade glioma growth. Given the better prognosis of lower grade glioma patients with high *SMPD3* expression, we focused further studies on *SMPD3,* which encodes for nSMase2, the major sphingomyelinase in the brain[39].

We next used the TCGA data to compare *SMPD3* expression levels in normal brain versus lower- and higher-grade gliomas. *SMPD3* expression levels were highest in normal brain, followed by lower-grade glioma and higher-grade GBM (Fig. 5D). We further dissected the lower-grade glioma dataset into IDH-mutant astrocytoma and IDH-mutant ODG and found that astrocytoma patients, which have a shorter survival time (median survival=9-13 years[6, 36]), presented with lower *SMPD3* transcript levels compared to ODG patients, which have a longer survival time (median survival= 12-14 years[40, 41]; Fig. 5E; $p<0.0001$) – suggesting that higher *SMPD3* levels may reduce tumor growth. Furthermore, within each disease type, patients with lower *SMPD3* expression in their tumors had shorter survival times compared to those with higher *SMPD3* expression (Fig. 5F, $p=0.0058$ for astrocytoma; and Fig. 5G, $p<0.0001$ for ODG; Table S1).

These data, together with our findings from our EV cell culture experiments (Fig. 2), suggest that higher *SMPD3* expression levels may limit ODG (and potentially also IDH-mutant astrocytoma) growth to a certain degree by triggering an increase in cytotoxic exosome production.

SMPD3* inhibits ODG proliferation *in vitro

To assess whether *SMPD3* might play a role in regulating ODG growth, we first confirmed that the encoded protein, nSMase2, was expressed in BT088 and BT054 ODG cells, demonstrating co-immunolabeling with Sox10, a marker of glial-like tumor cells[42] (Fig. S2A,B). Previous studies indicated that *SMPD3* overexpression enhances EV production[43], which our data suggested should inhibit ODG cell growth. To test this prediction, we used a doxycycline-inducible lentiviral system to generate stable *SMPD3*-GFP and control-GFP BT088 cell lines (Fig. 6A,A'). We confirmed that 72 hrs post-doxycycline exposure, nSMase2 expression was induced (Fig. 6B,B'). We also used nanoscale flow cytometry to confirm that *SMPD3* overexpression increased the release of $CD9^+$ EVs from *SMPD3*-GFP cells, revealing a 2.3-2.9 fold increase compared to control cells, and *SMPD3*-GFP cells not treated with doxycycline (Fig. 6C,C', Table S1).

We next monitored the growth of control-GFP and *SMPD3*-GFP BT088 cells using live cell fluorescent imaging of adherent cells (Fig. 6D-G'). As a proxy measure of cell growth, we monitored the cumulative area covered by GFP^+ cells normalized to seeding day (day 0) (Fig. 6H). Control-GFP cells and *SMPD3*-GFP cells not exposed to doxycycline grew exponentially, with doubling times in the range of 78-84 hrs. In contrast, doxycycline dosed *SMPD3*-GFP cells failed to proliferate in the first 1.5 days, after which there was a decline in the cumulative GFP area,

suggestive of cell death (Fig. 6H, Table S1). We also monitored the growth of Control-GFP and *SMPD3*-GFP BT088 cells grown in 3D suspension cultures, which can replicate more of the cell-cell interactions observed *in vivo*, and found that *SMPD3* overexpression similarly inhibits tumor cell growth (Fig. S2C-G). Finally, to assess the potential cytotoxicity of elevated *SMPD3* expression levels, we incorporated the cytotoxic dye 'Cytotox' in the culture media, and assessed the cumulative area covered by Cytotox$^+$ cells. Doxycycline dosed *SMPD3*-GFP cells increased Cytotox accumulation compared to all control conditions (Fig. 6I-M, Table S1).

Taken together with the cytotoxic nature of BT088 EVs on NSC and BT088 cell growth, we conclude that elevated *SMPD3* expression likely inhibits BT088 cell growth through the production of EVs, although we cannot rule out the potential for *SMPD3* having additional cell autonomous effects.

Knockdown of *SMPD3* promotes proliferation of ODG cells *in vitro*

We next asked the converse question, which is whether reduced *SMPD3* expression levels might promote ODG cell growth. We used an shRNA approach to stably knockdown *SMPD3* expression in BT088 cells. Lentiviral constructs that expressed GFP and one of four sh*SMPD3* variants (A-D) or an shScrambled (shScr) control sequence were transduced into BT088 cells to create five GFP-tagged BT088 cell lines (Fig. 7A). To assess the efficacy of sh*SMPD3* knockdown, we performed Western blotting, revealing a >50% decrease in nSMase2 levels for sh*SMPD3* B-D variants, but not variant A (Fig. 7B,B'). sh*SMPD3* variants B-D also all reduced the number of secreted CD9$^+$ EV particles compared to shScr control (Fig. 7C,C', Table S1). In addition, isolated EV pellets from the CM (from sh*SMPD3* B-D variants) had lower levels of Alix, an EV marker (Fig. S3A).

To assess the effects of *SMPD3* knockdown on BT088 cell growth, we used live cell fluorescent imaging of adherent cell cultures (Fig. 7D-H). Compared to shScr control cells, BT088 cells expressing sh*SMPD3* variants B-D cells grew more rapidly after 5 DIV, with doubling times of ~160-192 hrs compared to ~800 hrs for shScr control (Fig. 7H, Table S1). The growth stimulatory properties of *SMPD3* knockdown was similarly observed when BT088 cells were grown in 3D suspension cultures for 9 DIV (Fig. S3B-F). To further validate these data, we also performed manual tumorsphere counts and diameter measurements of BT088 cells expressing control shScr versus sh*SMPD3*-B (Fig. S3G-K). After 10 DIV, *SMPD3* knockdown increased tumorsphere number (Fig. S3I), tumorsphere size (Fig. S3J), and live cell number (Fig. S3K), replicating the live cell imaging data.

The increase in cell number observed after sh*SMPD3* knockdown could be due to an increase in proliferation and/or a decrease in cell death. Proliferation must have increased to produce more cells after sh*SMPD3* knockdown and, accordingly, all BT088 cell lines incorporated BrdU, indicative of active DNA synthesis in S-phase of the cell cycle (Fig. S3L-O). However, to determine whether *SMPD3* knockdown also reduced normal levels of cell death in BT088 cells, we assessed 'Cytotox' dye incorporation in BT088 cells expressing shScr versus sh*SMPD3* knockdown constructs, revealing more dye incorporation in the first days of culture by the sh*SMPD3* lines (Fig. 7I-M). Thus, knockdown of *SMPD3* expression in BT088 cells not only enhances cell proliferation, but also reduces cell death rates to increase tumor cell number.

As a final independent measure of the effects of *SMPD3* knockdown on BT088 cell growth, we used a pharmacological approach, treating BT088 cells with GW4869, a competitive inhibitor of phosphatidylserine, a phospholipid that binds nSMase2 and is required for enzyme activation[44, 45]. Exposure of BT088 cells to 1μM GW4869 for 48h reduced CD9$^+$ EV production by 2-fold

compared to DMSO control cells (Fig. S3P,Q). Treatment of BT088 cells with GW4869 also increased cell proliferation using live cell imaging but only at later stages (Fig. S3R-T). To confirm that the knockdown of *SMPD3* was stimulatory for BT088 growth, we also used a higher concentration of GW4869 (18 μM), which increased tumorsphere number (Fig. S3U-W) and size (Fig. S3X) after 5 DIV.

Taken together, we have genetic and pharmacological evidence that lowering *SMPD3* expression levels increases ODG cell proliferation and survival, in keeping with the reduced survival times associated with lower *SMPD3* expression in ODG patients.

SMPD3* knockdown facilitates ODG growth *in vivo

BT088 cells engineered to express GFP form tumors by 6 months after orthotopic xenograft into the cerebral cortices of NOD *scid* Gamma (NSG) mice (Fig. 8A). In the xenografts, the neoplastic (human) cells can be identified by the expression of human nuclear antigen (HNA) whereas mouse cells are negative for HNA (Fig. S4A,B). As expected, the main tumor masses were comprised predominantly of densely packed HNA^+ tumor cells, while a smaller number of HNA^+ tumor cells infiltrated at the periphery (Fig. S4A). We further confirmed that that engrafted HNA^+ BT088 cells continued to express nSMase2 (Fig. S4A,B).

We then used this model to further evaluate the impact of *SMPD3* expression on tumor growth in the context of the complex *in vivo* environment. We made stable *SMPD3* knockdown (KD) and shScr control BT088 cell lines (Fig. S4C-G). shScr and *SMPD3*-KD cells were orthotopically xenografted into NSG mice (N=8 per cohort), and animals were monitored over six months (Fig. 8A). shScr and *SMPD3*-KD BT088 survival curves were significantly different from one another (Fig. 8B; Mantel-Cox log rank test $p=0.0074$, Table S1). At endpoint, all mice were confirmed to have tumors in sections consisting of hypercellular masses that disrupted the normal cortical architecture. By day 154, however, all mice xenografted with *SMPD3*-KD BT088 cells had been sacrificed at the humane endpoint after showing terminal symptoms, whereas two mice xenografted with shScr BT088 cells were still alive after 6 months (181 days), our experimental endpoint.

To further characterize the tumor masses associated with BT088 shScr and *SMPD3*-KD cells, we co-immunostained sections with HNA along with the oligodendroglial lineage marker Olig2, the astrocytic marker GFAP, the vascular marker isolectin, and the proliferative cell marker Ki-67 (Fig. 8C-J). Both BT088 shScr and *SMPD3*-KD cells co-expressed HNA and Olig2 (Fig. 8C,D), as expected, and many HNA^+ tumor cells were Ki-67^+ in both tumor types (Fig. 8E,F). However, the two tumor types differed as *SMPD3*-KD tumors appeared to be more highly vascularized than control shScr tumors, with dense isolectin staining (Fig. 8G,H), phenocopying the increase vascular endothelial proliferation that is associated with higher-grade gliomas in patients[46]. In addition, $GFAP^+$ cells bearing morphologic features of reactive astrocytes (hypertrophy of soma and processes, resulting in coarser and enlarged processes, and more abundant cytoplasm) were more abundant in *SMPD3*-KD tumor margins (Fig. 8I,J), suggestive of enhanced reactive changes [47].

SMPD3 knockdown in BT088 cells thus results in the formation of more biologically aggressive tumors that display some phenotypic features of higher-grade III ODG[48].

***SMPD3* knockdown increases ODG invasiveness and growth in human cerebral organoids**

Tumor xenografting in immunocompromised mice is a powerful method to examine how genetic or pharmacological manipulations impact tumor burden, but species-specific features of

tumor growth cannot be examined. To test whether *SMPD3*-KD BT088 cells grew faster in a human context, we used cerebral organoids (COs) generated from human embryonic stem cells[49, 50]. Human COs have now been used in a few studies for brain tumor modelling and provide an excellent readout of tumor infiltration and growth progression[51]. To generate 30-day old COs, we followed a modified Lancaster protocol (Fig. S4H, 9A)[52]. After 30 DIV, COs were either cultured alone (Fig. 9B-B''') or together with BT088 cells for an additional 7 DIV (Fig. 9A,C-E'''). To assess *SMPD3* knockdown effects, we co-cultured 30 DIV COs with stable BT088 cell lines engineered to express GFP and shScr (Fig. 9A,C-C'''), sh*SMPD3*-B (Fig. 9A,D-D''') or sh*SMPD3*-D (Fig. 9A,E-E''') (knockdown validated; Fig. 7).

After 7 DIV, we first examined the neural identity of co-cultured COs by performing SOX2 immunostaining, which labeled neural rosettes in all COs (Fig. 9B'-E'). Notably, $SOX2^+$ rosettes tended to concentrate in the CO periphery, a positional preference that we validated by counting $SOX2^+$ cells in seven zones from periphery to the core (zone width =50 µm; Fig. 9A',F). The negative slope of the lines of best-fit suggested that there was a biased distribution of neural rosettes in the CO periphery, and as the slopes were similar for shScr, sh*SMPD3*-B and -D co-cultures, the addition of ODG cells did not alter neural cell organization (Fig. 9G; Table S1). Next, we co-stained the COs with turbo-GFP (tGFP) to label infiltrating tumor cells. $tGFP^+$ tumor cells were detected in all CO co-cultures (N=3 for each condition; Fig. 9B''-E''). Strikingly, for sh*SMPD3*-B and sh*SMPD3*-D BT088 lines, more $tGFP^+$ cells were detected in the periphery, where $SOX2^+$ neural rosettes localize, compared to shScr controls (Fig. 9H), as revealed by the significant difference in slopes of the lines of best-fit (Fig. 9I; Table S1). Moreover, *SMPD3* KD BT088 lines had more $tGFP^+$ cells in the CO compared to shScr, indicative of a growth advantage (Fig. 9J, Table S1).

Thus, the CO-tumor co-culture system recapitulated the more proliferative phenotype exhibited by sh*SMPD3* BT088 cells *in vitro* and in mouse xenografts.

DISCUSSION

ODG tumors are slow growing, but the molecular mechanisms underlying their indolent growth is poorly understood. Here we report that ODG cells produce cytotoxic EVs that could allow them to interact and communicate with other tumor cells and non-neoplastic brain cells in the glioma microenvironment. Furthermore, we identify *SMPD3* as a critical regulator of EV biogenesis in ODG tumors, revealing that lower *SMPD3* expression levels are associated with a less favourable prognostic outcome both in patients and in murine xenografts (Fig. 9K). Prior studies had demonstrated that EVs isolated from G26/24 ODG cells exerted a cytotoxic effect on neurons and astrocytes *in vitro,* acting via Fas ligand (Fas-L) and tumor necrosis factor-related apoptosis-inducing ligand (TRAIL), respectively[20, 21]. However, the *in vivo* relevance and underlying biogenetic pathways were not addressed. Moreover, it is important to acknowledge that G26/24 is a mouse glioma cell line that was originally classified as ODG based on histological resemblance[53]. G26/24 cells have not been shown to model the human disease genetically, and their relevance to human ODG remains unclear. Furthermore, while TRAIL and Fas-L mediate the cytotoxic effects of G26/24-EVs[20, 21], these factors were not present in BT088- and BT054- derived EVs, demonstrating key differences between mouse and human ODG EVs, while also highlighting the heterogenous nature of the ODG vesiculomes.

In aggregate, our data suggests that the secretion of cytotoxic EVs by ODG tumor cells may contribute to the slow growing nature of these tumors. Notably, *SMPD3* also exhibits growth inhibitory functions in other cancers, mediated either by its role in EV biogenesis or by its role in

ceramide production[54]. Early studies using a rat C6 glioma cell line found that *Smpd3* produces ceramide, which promotes apoptosis by activating PKCδ signaling[55]. Homozygous deletion of *Smpd3* also induces osteosarcoma in a rodent model[56]. In line with these studies, we report here that *SMPD3* inhibits ODG cell growth, possibly through paracrine and autocrine effects. Along with *SMPD3*, we also found a correlation between high expression levels of ESCRT-dependent exosome biogenesis genes[57] (*TSG101, STAM1*) and improved patient survival in low-grade glioma patients, suggesting that EV biogenesis via several pathways may play an important role in these tumors. It is important to note, however, that increasing EV biogenesis is not always favorable, and depends on the tumor type. For instance, knockdown of *Rab27a/b*, which also blocks EV secretion, was shown to inhibit tumor growth in other brain tumor models[58, 59]. *Rab27a/b* knockdown in astrocytes, which reduces EV secretion, blocks the metastasis of breast cancer cells to the brain[58]. Moreover, knockdown of *Rab27a/b* in an astrocyte-derived glioma cell line blocked glioma growth *in vivo* in mouse xenografts [59]. A likely cause of these different effects is that EV cargo is well known to differ based on the cell of origin[60]. In high-grade GBM tumors secrete EVs that contain many growth factors (e.g. EGFRvIII) that could promote glioma growth and progression[61, 62].

While we showed that ODG EVs have cytotoxic effects, it is likely not the EVs themselves that are cytotoxic, but rather, their enclosed cargo. Even within two different ODG lines, we found distinct differences between the vesiculomes that may help to explain differences in the growth of BT088 and BT054 cells. The identification of SRI (Sorcin) and MFGE8 (Lactadherin) in ODG cell EVs is of interest, as it suggested that VEGF signaling is increased, and indeed, we could block BT088 cell growth with Foretinib *in vitro*. VEGF signaling is typically linked to shaping the tumor vasculature, including in GBM [63], but our data is suggestive of a potential autocrine role for VEGF in supporting ODG growth, as has been suggested in GBM [64] and hepatocellular carcinomas [55]. Future studies in which ODG cell xenografted animals are treated with Foretinib would help assess the potential of this drug as a therapeutic, since *in vitro* assays are not always translated in an *in vivo* setting, as we have highlighted. Furthermore, the analysis of ODG EV-associated factors such as CLU, previously implicated in invasion[65], may help to understand how these tumor cells infiltrate the brain *in vivo*.

In summary, the mechanisms underlying neural-ODG cell interaction are complex with the tumor microenvironment playing a crucial role. Our studies indicate that ODG cells release EVs that serve as messengers of predominantly cytotoxic cargo to neighbouring cells. We further report that *SMPD3* expression levels correlate with ODG survival, and that *SMPD3* acts in part through its ability to regulate EV generation and secretion. Given that ODG EVs in the microenvironment contribute towards a slow growth phenotype, drugs that increase EV production could have therapeutic potential. While most high-throughput screens have focused on identifying small molecules that block EV secretion, which could be useful for GBM tumors[66], there have also been recent screens for small molecules that induce EV secretion[67]. Interestingly, N-methyldopamine and norepinephrine activate nSMase2 to increase EV production in mesenchymal stem cells (MSCs) without increasing cell number, a strategy that is being developed to enhance the regenerative potential of MSC EVs[67]. Testing whether these drugs increase ODG EV production and the associated cytotoxicity would be of interest in the future. However, one must keep in mind that it is also possible (likely) that the interaction of ODG EVs with non-neoplastic cells in the tumor niche may be reciprocated by EV secretion by brain cells that are not transformed, which together would help to create a unique microenvironment for every tumor. Careful analyses of drug efficacy would thus require 3D culture systems that mimic cell-cell interactions, such as our

human-CO/tumor cell co-culture assay, or xenografts into immunocompromised mice, which remains the gold standard for pre-clinical data.

METHODS

Patient-derived tumor tissues and cells and study approval. IDH mutant ODG and astrocytoma patient biopsies were obtained from the pathology archives at the Calgary Laboratory services and Clark Smith Brain Tumor Bank at the University of Calgary[9]. Samples were formalin fixed and embedded in paraffin. Approval for use was obtained from Calgary Laboratory Services and the Calgary Health Region Ethics Board (University of Calgary Conjoint Health Research Ethics Board to JAC (HREB #2875 and #24993). BT088 and BT054 cell lines were collected under approved protocols from the Health Research Ethics Board of Alberta to JAC (HREBA.CC-16-0762 and HREBBA.CC-16-0154). Culture of BT088 and BT054 cells was approved by the Sunnybrook Research Ethics Board (REB) to CS (PIN: 301-2017). Culture of human ESCs received approval from the Canadian Institutes of Health Research (CIHR) Stem Cell Oversight Committee (SCOC) to CS and was approved by the Sunnybrook REB (PIN: 264-2018).

The Cancer Genome Atlas (TCGA) survey. Kaplan Meier plot was generated from lowest and highest quartiles of all low-grade glioma patients for all assessed genes. Normal brain cortex (GTEX), GBM, low-grade glioma, IDH mutant astrocytoma, and IDH mutant ODG (TCGA) datasets were downloaded from UCSC's Xena Browser (https://xenabrowser.net/) and analyzed to compare *SMPD3* expression levels, which was correlated with overall patient survival.

Animals. CD1 outbred mice used for neurosphere assays were purchased from Charles River Laboratories (Senneville, QC). Embryos were staged using the morning of the vaginal plug as embryonic day (E) 0.5. Sex was not considered due to the difficulty in assigning sex at embryonic stages. Animal procedures were approved by the Sunnybrook Research Institute Animal Care Committee (20-606) in compliance with the Guidelines of the Canadian Council of Animal Care.

BT088 and BT054 cell culture. BT088 and BT054 cells[9] were grown in Human Neurocult proliferation media (Stem Cell Tech; # 05751) containing human epidermal growth factor (hEGF, 20 ng/ml, Peprotech; AF-100-15), human fibroblast growth factor 2 (hFGF2, 20 ng/ml, Wisent; # 511-126-QU), heparin (2 µg/ml; Stem Cell Tech, #07980), and Antibiotic-Antimycotic solution (0.1%; Wisent; # 05751). Tumorspheres were dissociated and passaged using Accutase (Stem Cell Tech; # 07920). Neurosphere media was DMEM (Wisent; #319-005-CL):F12 (ThermoFisher Scientific; #31765-035) (3:1), with hFGF2 (20ng/ml), hEGF (20ng/ml), B27 supplement (2%; ThermoFisher Scientific; #17504044), Antibiotic-Antimycotic solution (0.1%), Cyclopamine (0.5 µM; Sigma; #C4116), and Heparin (2 µg/ml). BT088 cells were cultured either as adherent cells on Poly-D-Lysine:Laminin coated tissue culture plates, or in suspension on non-coated flasks/plates. For BT088 tumorsphere assays, dissociated BT088 cells were seeded at 8000 cells/ml in BT088 media (FM), or in BT088 FM+EVs. BT088 cells grew undisturbed for 5 DIV, and tumorspheres were then imaged.

Small molecule inhibitors. Small molecules were added as follows: GW4869 (stock concentration=1 mM): FM was supplemented with 1 or 18 µl/ml DMSO (control) or 1 µl/ml of 1 µM or 18 µl of 18 µM GW4869 (SigmaAldrich). Foretinib (stock concentration=0.1 mM): FM

was supplemented with 5 µl/ml DMSO (control) or 0.5, 1, 2, 4 or 5 µl/ml Foretinib (GSK1363089) at 50, 100, 200, 400, or 500 nM.

Mouse NSC isolation and culture. Dorsal telencephalons (cortices) from E13.5 embryos were dissected and dissociated in 0.125% trypsin (Wisent) at 37°C for 10 mins. Dissociated cells were seeded at 8000 cells/ml in neurosphere media (FM), or in BT088 or BT054 CM, CM-EV, or FM+EVs. NSCs grew undisturbed for 7 DIV, and neurospheres were then imaged.

AnnexinV- PI Apoptosis assay. NSCs were cultured in FM, BT088 CM, CM-EV, and FM+EV for 3 DIV. Cells were stained with FITC-labeled Annexin V and PI using the FITC Annexin V Apoptosis Detection Kit with PI as per the manufacturer's instructions (BD Biosciences; 640914) for 20 min at 25˚C and analyzed by flow cytometry.

Conditioned media. $1x10^6$ BT088 or BT054 cells were seeded in 11 ml of fresh media and CM was collected after 24 hrs. CM was centrifuged at 300 x g for 5 min to remove cells, followed by 2000 x g for 10 min to remove cellular debris and 10,000 x g for 30 min to remove protein aggregates and smaller debris. CM was then sequentially ultra-centrifuged at 100,000 x g at 4˚C for 2 hrs in a Beckman Coulter Optima L-100 XP Ultracentrifuge using an SW41-Ti rotor and polycarbonate centrifugation tubes (Beckman Coulter; #331372). The EV pellet, and supernatant (CM-EV) were used as indicated. The EV pellet was rinsed with Phosphate Buffered Saline (PBS) (ThermoFisher Scientific; # 14190144) and centrifuged at 100,000 x g, 4˚C for 1 hr and resuspended in 50 µl PBS prior to use.

Incucyte live cell imaging. Cell growth and death were monitored using an Incucyte S3 Live cell imaging system (Essen BioScience). BT088 and BT054 cell growth rates were monitored using NucLight Rapid Red Reagent for nuclear staining of the cells (as per manufacturer's instructions; IncuCyte; #4717). Cells were suspended in media supplemented with 2 µl/ml of the reagent prior to cell seeding. Cell growth was quantified by monitoring area covered by RFP+ objects. All other cell growth studies monitored total phase area confluence or area covered by GFP+ cells. For cell death assays, the media was supplemented with 0.25 µl/ml of Cytotox dye/well (as per manufacturer's instructions; red #4632 and green #4633) prior to cell seeding. Phase contrast and Red/Green fluorescent imaging was carried out at designated intervals (cell growth studies: every 12/24 hrs; cell death studies: every 4/12 hrs), and at 10x/20x magnification. A minimum of 9 images were taken per well at each time point. Quantification of cell proliferation and cell death was performed using the analyser algorithm built in the Incucyte application. Mean values of total phase area (normalized to day 0) ratio (U) and $Cytotox^+$ object area (normalized to day 0) ratio (V) were plotted, comparing between days 0 to 7.

CO-BT088 co-cultures. Feeder-free H1 hESCs (WiCell) were cultured on Matrigel in TeSR™-E8™ kit for hESC/hiPSC maintenance (StemCell Tech; #05990). hESCs were used to generate COs using media included in the STEMdiff Cerebral Organoid Kit (StemCell Tech; #08570) and STEMdiff Cerebral Organoid Maturation Kit (StemCell Tech; #08571), with some modifications. Briefly, hESCs were plated in 96-well round-bottom ultra-low attachment plates at 9,000 cells/well in embryoid body (EB) seeding medium. Dual SMAD inhibitors (2µM Dorsomorphin; StemCell Tech; #72102, and 2 µM A83-01; StemCell Tech; #72022) until day 5. Newly formed EBs were transferred to 24-well plates containing StemCell Tech CO induction medium. On day 9, EBs with

optically translucent edges were embedded in matrigel and deposited into 6-well ultra-low adherent plate with StemCell Tech expansion medium. From day 5 to day 13, media was supplemented with 1 μM CHIR-99021 (StemCell Tech; #72052) and 1 μM SB-431542 (StemCell Tech; #72232) to support formation of well-defined, polarized neuroepithelia-like structures. On day 13, embedded EBs exhibiting expanded neuroepithelia as budding surfaces were transferred to a 12-well spinning bioreactor (Spin Omega[52]) containing maturation medium in a 37°C incubator. For BT088 co-culture, on day 30, COs were individually transferred to a 24-well plate containing Neurocult NS-A proliferation media (Catalog # 05751, StemCell Tech) with freshly added hFGF2 (20 ng/ml), hEGF (20ng/ml), and heparin (2μg/mL). Subsequently, 10,000 GFP^+ BT088 cells were added to each well. Plates were incubated for 24 hrs without agitation and on the next day tumor-bearing COs were washed with PBS once and maintained in maturation media on an orbital shaker at 37°C for 7 more days. On day 8, COs were fixed in 4% paraformaldehyde (PFA) for 45 min, transferred into 30% sucrose overnight, snap frozen in OCT for cryosectioning.

Pellet assay. BT088 cells expressing GFP and Cre were mixed with NIH-3T3 cells transfected with BFP-loxP-dsRed in a 5:1 ratio. Cells were centrifuged, and the pellet was placed on a cell culture membrane. The membrane was floated on DMEM media in a 6-chamber dish. The cells were incubated at 37˚C for 3DIV after which the membrane was embedded in a cryopreservative, OCT, and frozen gradually on dry ice. 10 μm thick sections were obtained by sectioning the OCT block.

Density gradient Ultracentrifugation. OptiPrep™ (Iodixanol 60% stock solution; StemCellTech; #07820) was diluted with a homogenization solution (0.25M sucrose in 10mM Tris HCl pH 7.5) to generate a discontinuous density gradient of 40% (2.5ml), 20% (2.5ml), 10% (2.5 ml), and 5% (2 ml). The solutions were carefully pipetted in an ultracentrifuge tube and left undisturbed for >1hr. EVs (filtered through a 0.2 μm filter and resuspended in 500 μl PBS) isolated from BT088 CM by sequential centrifugation after the first 100,000 x g spin were loaded onto the gradient. Samples were centrifuged at 100,000 x g for 18 hrs. Post centrifugation, 1 mL fractions were pipetted out carefully from the top. Fractions were mixed with PBS and centrifuged at 100,000 x g for 4 hrs. EV pellets were resuspended in 50 μl PBS.

Scanning Electron Microscopy. BT088 and BT054 cells were cultured on 13 mm coverslips (EM Biosciences) precoated with Poly-O-Lysine – Laminin in a 24 well plate. The samples were then fixed (2% glutaraldehyde in 0.1M sodium cacodylate buffer, pH 7.3; for >2 hrs), rinsed and dehydrated. Samples were mounted on stubs, gold sputter-coated, and imaged with FEI/Philips XL30 scanning electron microscope at 15 kV. Imaging was performed in the Nanoscale Biomedical Imaging Facility, SickKids Research Institute.

Transmission Electron Microscopy. Before grids were prepared, carbon-coated Cu400 TEM grids were glow discharged for 30 s (Pelco EasiGlow, Ted Pella Inc.). Then 4 μL of BT088 exosome solution was applied to the grid for 60 seconds before wicking away excess solution. The grid was washed three times with 4 μL of distilled water. The grid was stained with 4 μL of 2% uranyl acetate solution for 30 seconds. Excess uranyl acetate solution was wicked away. The grids were air-dried. Imaging was performed on a Thermo Fisher Scientific Talos L120C TEM operated

at 120 kV using a LaB6 filament. Imaging was performed in the Microscopy Imaging Laboratory, University of Toronto.

Nanosight tracking analysis (NTA) and Nano-flow cytometry. NTA was performed using the Malvern NanoSight NS300 at the Structural & Biophysical Core Facility, University of Toronto. EV pellets were collected by sequential centrifugation, resuspended in 200 µl PBS, diluted 1:50 and passed through the Nanosight chamber. NTA data acquisition settings were as follows: camera level 13, acquisition time 3 × 30 s with detection threshold 12. Data was analyzed with the NTA 3.2 Dev Build 3.2.16 software. For nanoscale flow cytometry, EVs (1 µl in 18 µl sterile water) were incubated with CD9 antibody (1 µl; Santa Cruz; #sc9148) for 30 mins at room temperature. Post incubation, EVs were stained with Alexa Fluor 647 Far red secondary antibody (1 µl of 1:20 antibody solution; Invitrogen) for 20 mins. Stained EVs were diluted in 500 µl sterile water and quantified on the Nanoscale Flow Cytometer (Apogee Flow Systems Inc). Representative scatterplot of BT088 EVs plotted for 638-Red (detecting Alexa 647 bound $CD9^+$ particles) and Long angle light scatter (LALS; for size distribution) EVs were defined as size events greater than 100 nm.

Molecular Cloning. <u>*SMPD3* Gain of function:</u> Conditional overexpression of *SMPD3* was achieved with a doxycycline inducible lentiviral vector pCW57-MCS1-P2A-MCS2 (GFP) (Addgene plasmid # 80924). We cloned *SMPD3* (*SMPD3* Human Tagged ORF Clone, Origene Cat#: RG218441, RefSeq- NM_018667.2) and, after the P2A site, *Luc2* (pcDNA3.1(+)/Luc2=tdT (Addgene plasmid # 32904)) into this vector. <u>*SMPD3* Loss of function</u>: For all *in vitro SMPD3* knockdown experiments, we used NSMase2 (SMPD3) Human shRNA Plasmid Kit (Origene, Locus ID 55512), which included what we termed sh*SMPD3* variants A-D and shScr. For xenograft experiments, we used a piggyBac shRNA (GFP) construct (SB #PBSI505A-1) as the backbone. The vector backbone was linearized with *BamH*1 and *EcoR*1 and the following annealed oligonucleotides were cloned into the site:
<u>sh*Smpd3*</u>:5'pGATCCCCCTCATCTTCCCATGTTACTTCAAGAGAGTAACATGGGAAGAT GAGGGACGCGTG3'(sense) and 5'pAATTCACGCGTCCCTCATCTTCCCATGTTACTC TCTTGA AGTAACATGGGAAGATGAGGGG 3' (antisense); and for shScrambled:
5'pGATCCATTCACTTATCCGCCTCTCCTTCAAGAGAGGAGAGGCGGATAAGTGAATC TCGAGG3'(sense), and 5'pGAATTCCTCGAGATTCACTTATCCGCCTCTCCTCTCTTGAA GGAGAGGCGGATAAGTGAATG -3' (antisense). The sh*Smpd3* construct targeted mouse *Smpd3* sequence, such that the mouse shRNA target sequence has a 3 bp mismatch upon alignment with human *SMPD3* sequence, but it effectively knocked down human *SMPD3* (Fig. S4A).

Transduction and transfection. <u>*SMPD3* Gain of function:</u> To generate lentiviral particles for *SMPD3*-P2A-Luc2 GFP and Luc2 GFP the lentiviral vector was packaged in LentiX HEK293T cells using the packaging plasmids psPAX2 (Addgene Plasmid #12260) and pMD2.G (Addgene Plasmid #12259). The resulting lentiviral particles were concentrated by ultra-centrifugation and used to transduce BT088 cells. To induce *SMPD3*-Luc2 or Luc2 only (control) expression, transduced GFP^+ cells were treated with 2 µg/mL doxycycline hyclate (D9891, Sigma). <u>*SMPD3* Loss of function</u>: BT088 cells were transduced with 4 *SMPD3* human shRNA lentiviral particles (A,B,C,D) and Lenti shRNA Scramble control particles (pGFP-c-shLenti; TL301492V; Origene). Transduced GFP^+ cells (sh*SMPD3*-GFP variants B,D and shScrambled-GFP) used in CO co-culture studies were sorted using the BD FACS ARIA III. GFP^+ cells were selected and collected

in Neurocult proliferation media and plated. For *in vitro* tumorsphere assays and generating BT088 cells for xenograft studies, BT088 cells were nucleofected with each sh*Smpd3*/shScrambled vector mixed with Super PiggyBac Transposase expression vector (SBI, Cat#PB210PA-1) in 1: 3, PiggyBac: transposase ratio. $2x10^6$ dissociated BT088 cells were suspended in 20 µl of P3 reagent with the DNA mix (final concentration=12 µg). Nucleofection was performed using the 4D nucleofector (Lonza) in nucleofector strips using the program CZ167. For shSmpd3 knockdown experiments, HEK 293 LentiX cells were transfected with Super PiggyBac Transposase expression vector, h*SMPD3*-GFP construct, and shScr/sh*SMPD3* (internal control)/ or mouse sh*Smpd3*-GFP construct using Lipofectamine 3000 (ThermoFisher).

Tumor xenografts. sh*Smpd3*-GFP and shScr-GFP BT088 were injected into the right cerebral hemispheres of 8-10-week old female NOD *scid* Gamma mice (NSG; NOD.Cg-Prkdc^{scid} *Il2rg*^{tm1Wjl}/SzJ; N=8) (Princess Margaret animal breeding facility). Coordinates for implantation were AP-1.0, ML 2.0, and DV 3.0. The xenografted cells developed into tumors, for which the mice were monitored daily. Upon development of terminal symptoms, mice were sacrificed at relative end points. Two control mice did not show any terminal symptoms post engraftment and were humanely sacrificed after 180 days.

Western blotting. Cell or EV pellets were lysed in lysis buffer with protease (1X protease inhibitor complete, 1 mM phenylmethylsulfonyl fluoride) and phosphatase (50 mM NaF, 1 mM NaOV) inhibitors. 3-10 µg of lysate was run on 10% SDS-PAGE gels for Western blot analysis. Primary antibodies included: Flotillin1 (Cell signalling; #3253), CD9 (Santa Crutz; #sc9148), nSMase2 (Abcam; #ab85017), Cetp (Abcam; #ab2726), Alix (Cell Signaling; #2171S), GM130 (BD Biosciences; #610822), Calnexin (Abcam; #ab22595), Calreticulin (Abcam; #ab2907), Pex5 (Novus Biologicals; #NBP1-87185), VDAC (Cell Signaling; #4661), and Actin (Abcam; #ab8227). Densitometries were calculated using ImageJ. The average values of normalized expression levels were plotted.

Tissue Processing and Immunostaining. ODG patient tumor sections were stained using the Opal™ 4-Color Manual IHC Kit (NEL820001KT), as per manufacturer's instructions. In case of tumor xenograft studies, upon reaching end-time mice were sacrificed and perfused with PBS and 4% PFA solution. Mouse brains were collected and fixed at room temperature for 30 mins. The samples were then rinsed with PBS and immersed in 20% sucrose overnight at 4°C and embedded in OCT. 10 µM cryosections were collected on Superfrost Plus slides (Fisher). For immunostaining, sections were washed and permeabilized in Phosphate Buffered Saline with 0.1% Triton X100 (PBT) followed by blocking with 10% normal horse serum/PBT (blocking solution) for 1 hr at room temperature. Sections were then incubated with primary antibodies overnight at 4°C. Sections were washed with PBT and incubated with secondary antibody for 1 hr at room temperature. Sections were then washed and counterstained with DAPI diluted in PBT at room temperature. Sections were washed in PBS and mounted with coverslips using AquaPolymount (Polysciences). Primary antibodies included: pERK (Cell Signaling; #CS4370S); IDH1 R132H (Dianova; #DIA-H09) ; Ki67 (Abcam; #ab16667); GFAP (Millipore; #mab360) ; Olig2 (Abcam; #ab109816), Sox2 (Abcam; #ab97959) HNA (Millipore; #MAB1281), nSMase2 (Abcam; #ab85017), CD63 (Abcam; #ab59479); turboGFP (Origene; #TA150041), BrdU (Abcam;

#ab6326). Secondary antibodies included: Alexa 568 donkey anti-rabbit, Alexa 488 donkey anti-rabbit, Alexa 488 donkey anti-mouse (all from Invitrogen), and were diluted in PBT.

Mass Spectrometry. Mass spectrometry was performed on BT088 and BT054 EVs isolated by sequential ultracentrifugation at the SPARC Biocentre-Mass Spectrometry facility at SickKids Research Institute. Mass spectrometry analysis information is provided in Table S3. Scaffold data analysis was performed by applying NCBI annotations to all proteins, removing proteins that matched the search term "keratin" and which did not have "Homo sapiens" under the taxonomy heading. Protein filtering thresholds were set at 99.0%, with a minimum number of 2 peptides and a peptide threshold of 95%. For analysing the EV samples, Cytoscape program and ClueGO plugin were used.

Image analysis. Images were captured with a Leica DM IL LED or DMRXA2 optical microscope using LasX software. ImageJ software was used for image analysis. For astrocytoma and ODG patient tumor analysis, Single channel TIFF images with pERK/Ki-67/OLIG2 staining from all sample sets were transformed to binary format with mean intensity as the selecting parameter. A fixed minimum and maximum threshold value were determined for each set of images to ensure correct thresholding of pERK/Ki-67/OLIG2 staining. Images were analyzed by adjusting the size filter option to count cells with pERK or Ki-67 staining giving the total number of $pERK^+$/ $Ki\text{-}67^+$/ $OLIG2^+$ cells in each data set. Single channel images with pERK/Ki-67/OLIG2 staining were merged with IDH1 R132H (IDHm) single channel images. Cells displaying co-localization of pERK/Ki-67/OLIG2 with IDHm was manually counted. For primary neurosphere and tumorsphere assays, neurosphere/tumorsphere sizes were measured using the ruler measurement tool in ImageJ. For cerebral organoid-tumor co-culture assessment, zone-wise cumulative GFP intensity and total number of $Sox2^+$ cells were analyzed using ImageJ. The freeline tool was used to mark the periphery of the organoid. Seven zones (width=150 pixels or 50 µm) were constructed mapping the shape of each organoid, spanning from organoid periphery (zone1) to the core (zone7). Cumulative GFP intensity and $Sox2^+$ cell counts were assessed per zone.

Statistical analysis. A minimum of three biological replicates were carried out for all assays. Statistical analysis and graphs were generated using GraphPad Prism 6 software. Student's t-test was used when comparing two groups, while One-way ANOVA with TUKEY post corrections were used when comparing groups of more than two. All data expressed as mean value ± standard error of the mean (SEM). In all experiments, a p value <0.05 was taken as statistically significant, $*p < 0.05$, $**p < 0.01$, $***p < 0.005$, and $****p < 0.001$.

ACKNOWLEDGEMENTS
We thank Dr. Gregory Cairncross and Dr. Sam Weiss (University of Calgary) for providing the BT088 and BT054 tumor cell lines for our study. We thank Ali Darbandi (TEM), Lindsey Fiddes (SEM) and Greg Wasney (NTA) for technical help. This project was supported by an International Development Research Centre (IDRC 108875) to CS, Canada First Research Excellence Fund (CFREF) Medicine by Design Cycle 2 to CS and CM, and a Cancer Research Society grant to CS and JAC. CS holds the Dixon Family Chair in Ophthalmology Research.

AUTHOR CONTRIBUTIONS
AB: conceptualization, data curation, formal analysis, investigation, methodology, visualization, validation, writing – original draft, writing – review and editing

LA: conceptualization, data curation, formal analysis, investigation, methodology, visualization, validation, writing – review and editing
VC: conceptualization, data curation, formal analysis, investigation, methodology, visualization, validation, writing – review and editing
LV: data curation, formal analysis, software
OP: data curation, formal analysis, software
MJC: data curation, formal analysis, investigation
AES: data curation, formal analysis, investigation
TO: formal analyses, software, validation
YT: formal analysis, methodology
STA: formal analysis, software
RI: methodology, investigation
DZ: methodology, investigation
SS: formal analysis, methodology
LCC: formal analysis, methodology
BK: formal analysis, methodology
TF: methodology, investigation
HSL: resources, supervision, writing – review and editing
CMM: resources, supervision, writing – review and editing
MB: resources, supervision, writing – review and editing
VAW: resources, supervision, writing – review and editing
JAC: resources, supervision, validation, writing – review and editing
CS: funding acquisition, conceptualization, project administration, resources, supervision, validation, writing – original draft; writing – review and editing

COMPETING FINANCIAL INTERESTS.
The authors declare no competing financial interests.

FIGURE LEGENDS

Figure 1. IDH mutant oligodendroglioma display non-cell autonomous activation of proliferation and receptor tyrosine kinase signaling.

A-J. ODG patient sections co-immunostained with IDHm and OLIG2 (A-D") or Ki-67 (F-I"). Blue is DAPI counterstain. Yellow arrows indicate IDHm$^-$ cells that are OLIG2$^+$ or Ki-67$^+$. Percentage of OLIG2$^+$/Ki-67$^+$ IDHm$^-$ and OLIG2$^+$/Ki-67$^+$ IDHm$^+$ cells (E,J,) in oligodendroglioma patients. Regions marked with white dotted boxes in A,C,G,I,M,O were digitally magnified (4 times) and presented in B-B",D-D",G-G",I-I". **K.** Tumor microenvironment is composed of tumor cells and non-neoplastic neural cells (astrocytes, neurons, microglia, oligodendrocyte, endothelial cells). Vesicular and/or non-vesicular factors (represented as small spheres) may mediate inter-cellular communication in the tumor microenvironment. Bars represent means ± s.e.m.. Scale bars: 200 μm.

Figure 2. Patient-derived oligodendroglioma cells secrete soluble and EV-enclosed bioactive factors.

A. Live cell imaging of BT088 and BT054 cell growth, monitoring expansion of NucLight Rapid Red-stained cells over 10 days *in vitro*. **B.** Experimental setup to assess the bioactivity of the

BT088 and BT054 secretome. **C-J.** E12.5 NSCs grown in fresh media (FM; C), BT088 conditioned media (CM; D), conditioned media without EVs (CM-EV; E), and fresh media with EVs (FM+EV; F) for 7 DIV (G). Quantitation of BT088 neurosphere number (H), neurosphere size (I), and live cell number (J). **K-N.** E12.5 NSCs grown in FM, BT054 CM, CM-EV, and FM+EVs for 7 DIV (K). Quantitation of BT054 neurosphere number (L), neurosphere size (M), and live cell number (N). **O-S.** BT088 cells grown in BT088 FM (O,P) and BT088 FM+EVs (O,Q) for 5 DIV. Quantitation of tumorsphere size (R), and live cell number (S). **T-V.** Live cell imaging of NSCs grown in FM, BT088 CM, CM-EV, FM+EV (T), monitoring growth (U) and dying cells labeled with Cytotox dye (V). Bars represent means ± s.e.m.. **, $p < 0.05$; **, $p < 0.01$; ***, $p < 0.005$*. Scale bars: 100 µm in (C-F), 50 µm in (P,Q).

Figure 3. Bioactive exosomes are secreted from oligodendroglioma cell lines.

A,B. Scanning EM of BT054 (A) and BT088 (B) cells. Red arrows mark vesicles. **C,C'.** Transmission electron microscopy of BT088 EVs. Higher magnification image shown in (C'). **D-G.** Nanosight tracking analysis of BT054 and BT088 EVs isolated by sequential ultracentrifugation (D,E) and density gradient ultracentrifugation (fraction 4; F). $CD9^+$ EVs analyzed using nanoscale flow cytometry (G). **H-J.** Western blots of BT088 whole-cell lysates (CL) and EV lysates obtained by sequential ultracentrifugation, analyzed for the expression of EV markers (Alix, CD9, Cetp, Flotillin1) (H) and Calreticulin, Calnexin (ER), GM130 (Golgi body), Vdac (mitochondria), and Pex5 (Peroxisomes) (I). Density gradient ultracentrifugation of BT088 EVs, with 8 fractions analysed by Western blots for Alix, CD9, Cetp, Calnexin, and Vdac. **K-O.** Schematic of pellet assay mixing BT088 cells expressing Cre-GFP at 5:1 ratio with NIH-3T3 cells expressing a dual BFP-loxP-dsRed reporter (K). Analysis of GFP (L,M), BFP (L,N) and dsRed (L,O) expression in pellets after 3 DIV. White arrows mark $dsRed^+BFP^-GFP^-$ cells. White arrowheads mark $dsRed^+BFP^+GFP^-$ cells. Scale bars: 2 µm in (A,B); 500 nm in (C); 50 nm in (C').

Figure 4. Proteomic profiling reveals distinct BT088 and BT054 vesiculomes and identifies VEGF signaling as a targetable growth-promoting pathway.

A. GO term enrichment network of all proteins enriched in BT088 (green) and BT054 EVs (beige). **A'.** Commonly expressed proteins in BT088 and BT054 vesiculomes. **B.** GO terms relating to biological processes plotted against percentage of proteins identified in BT088 vs BT054 EVs**. C-L.** Relative levels of proteins enriched in BT088 versus BT054 cell derived EVs, comparing RHOA (C), RPL11 (D), HTRA1 (E), CLU(F), PKM (G), HSPB1 (H), HSP90AA1 (I), HSP90AB1 (J), SRI (K), and MFGE8 (L). **M,N.** Live cell imaging of BT088 cells treated with Foretinib (50-500nM) and DMSO control. Growth was assessed by calculating total phase area (M) and cell death by calculating total $Cytotox^+$ area (N), both normalized to day 0. Bars represent means ± s.e.m..

Figure 5. Poor prognosis in oligodendroglioma patients associated with low *SMPD3*.

A-C. Kaplan–Meier survival curves for correlation between *SMPD3* (A)*, TSG101* (B)*, STAM1* (C) expression and survival in low-grade glioma patients (Log-rank (Mantel-Cox) test; $p<0.0001$). **D.** *SMPD3* levels are higher in normal brain cortex compared to low-grade gliomas and GBMs. **E.** *SMPD3* levels are higher in ODG tumors versus astrocytoma. $p<0.0001$. **F.** Kaplan–Meier survival curves for correlation between *SMPD3* expression and survival of astrocytoma patients. Log-rank (Mantel-Cox) test; $\chi^2=7.601$; $p=0.0058$; high *SMPD3*>15.81 (n=66); low *SMPD3*<15.0 (n=65). **G.** Kaplan–Meier survival curves for correlation between *SMPD3* expression and survival of ODG

patients. Log-rank (Mantel-Cox) test; χ^2=15.27; *p<0.0001*; high *SMPD3*≥16.96 (n=66); low *SMPD3*≤16.28 (n=66). ****, *p < 0.0001.*

Figure 6. High *SMPD3* expression inhibits oligodendroglioma cell growth.

A-C'. Generation of doxycycline-inducible system to assess the effects of *SMPD3* on BT088 cell growth, showing Ctrl-GFP (A) and *SMPD3*-GFP (B) cells. Western blotting showing relative nSMase2 expression normalized to Actin (B,B'). Analysis of $CD9^+$ EV particle number using nano-flow cytometry in Ctrl-GFP and *SMPD3*-GFP cells (C,C'). **D-H.** Live cell imaging to monitor growth of Ctrl-GFP and *SMPD3*-GFP cells, showing growth with and without doxycline at day 0 (D-G) and day 5 (D'-G'). Quantitation of cell growth (normalized to day 0) (H). **I-M.** Live cell imaging of Cytotox dye labeled Ctrl-GFP and *SMPD3*-GFP cells to monitor induction of cell death, showing growth without (I-L) and with (I'-L') doxycycline at days 1, 2, 3, and 5. Quantitation of $Cytotox^+$ cells (normalized to day 0) (M). Bars represent means ± s.e.m.. *, *p < 0.05;* **, *p < 0.01. p*-values for all points in H and M in Table S1. Scale bars: 200 µm.

Figure 7. Low *SMPD3* expression promotes oligodendroglioma cell growth.

A-C'. Use of shRNA constructs to assess the effects of *SMPD3* knockdown on BT088 cell growth, depicting shScr and sh*SMPD3* (variant A,B,C,D) constructs (A). Western blotting showing relative nSMase2 expression normalized to Actin (B,B'). Analysis of $CD9^+$ EV particle number using nano-flow cytometry in shScr and sh*SMPD3* (variant A,B,C,D) BT088 cells (C,C'). **D-H.** Live cell imaging to monitor growth of shScr and sh*SMPD3* (variant A,B,C,D) BT088 cells at day 0 (D-G) and day 5 (D'-G'). Quantitation of cell growth (normalized to day 0) (H). **I-M.** Live cell imaging of Cytotox dye labeled shScr and sh*SMPD3* (variant A,B,C,D) BT088 cells to monitor induction of cell death, showing $Cytotox^+$ cells at day 0 (I-L) and day 5 (I'-L'). Quantitation of $Cytotox^+$ cells (normalized to day 0) (M). Bars represent means ± s.e.m.. *, *p < 0.05;* **, *p < 0.01. p*-values for all points in H and M in Table S1. Scale bars: 200 µm.

Figure 8. *SMPD3* knockdown facilitates oligodendroglioma growth *in vivo*.

A. Schematic of xenografting protocol, showing NSG mice were xenografted with shScr and *SMPD3*-KD BT088 cells and tumor growth was monitored. **B.** Kaplan–Meier survival curves associated with shScr and *SMPD3* KD BT088 cell xenografts. Log-rank (Mantel-Cox) test; χ^2=7.162; *p=0.0074.* **C-J.** Co-immunostaining of shScr (C,E,G,I) and *SMPD3* KD (D,F,H,J) BT088 cell xenografted tumors with HNA (red) and Olig2 (green, C,D), Ki-67 (green, E,F), Isolectin (green, G,H), and Gfap (green, I,J). Blue is DAPI counterstain. Insets present split channel images of regions marked by a dotted box. Br, normal brain; xe, xenograft. Scale bars: 50 µm in (C-J).

Figure 9. *SMPD3* knockdown facilitates oligodendroglioma growth in human cerebral organoids.

A-A'. Schematic of cerebral organoid (CO)- BT088 co-culture assay, depicting 30-day old hESC-derived COs co-cultured with BT088 cells (shScr, sh*SMPD3*-B/D) for 7 DIV (A). Quantitation method, depicting division of each CO into 7 zones spanning organoid periphery to the core (0-350 µm) (A'). **B-E'''.** Immunostaining of COs grown alone or in CO-BT088 co-cultures with SOX2 (red, B-E, white, B'-E') and turbo GFP (t-GFP; green, B-E, white, B''-E''). Blue is DAPI

counterstain (B-E, white, B'''-E'''). **F.** Percentage of SOX2 $^{+}$ cells in each of 7 zones. **G.** Lines of best-fit from (F) plotted for the three conditions. shScr: slope= -0.04789 ± 0.003408; sh*SMPD3*-B: slope= -0.02941 ± 0.007366, *p= 0.1234;* sh*SMPD3*-D: slope= -0.03215 ± 0.003388, *p= 0.2205* **H.** Percentage of t-GFP intensity per zone per section. **I.** Lines of best-fit from (H) plotted for shScr: slope= -0.01259 ± 0.003080; sh*SMPD3*-B*:* slope= -0.02711 ± 0.001588, *p= 0.003646*; sh*SMPD3*-D*:* slope= -0.03269 ± 0.004513, *p= 0.000118.* **J.** Cumulative t-GFP intensity/unit area in shScr and sh*SMPD3*-CO sections*.* **K.** Summary of major findings: *SMPD3* expression in the brain is high under normal healthy conditions. ODG cells with high *SMPD3* expression produce more EVs and grow slower. ODG cells with low *SMPD3* expression produce less EVs and grow faster. **, p < 0.05; ***, p < 0.005*. Scale bars: 100 µm.

Table 1. Summary of ODG patient tumors analyzed. Five ODG patient tumors used for the study.

Supplementary Fig. 1. Oligodendroglioma EVs induce apoptosis in neural stem cells.

A-E. ODG patient biopsies co-immunostained with IDHm and pERK (A-D''). Blue is DAPI counterstain. Yellow arrows indicate IDHm^{-} cells that are pERK^{+}. Percentage of pERK $^{+}$ IDHm^{-} and pERK $^{+}$ IDHm^{+} cells (E) in oligodendroglioma patients. Regions marked with white dotted boxes in A,C were digitally magnified (4 times) and presented in B-B'',D-D''. **F-Q**. Representative images of Cytotox incorporation in NSCs exposed to FM, CM, CM-EV, FM+EV at day 0,5,7 from one independent experiment. **R.** NSCs were cultured in FM, BT088 CM, CM-EV, and FM+EV for 3 DIV. Cells were stained with FITC-labeled Annexin V and propidium iodide (PI) and analyzed by flow cytometry. A typical flow cytometry dot plot from one representative experiment is given for each sample. Cell death was determined by quadrant gating: Q1 (necrotic cells); Q2 (late apoptotic cells); Q3 (early apoptotic cells); Q4 (live cells). **S**. Mean values of Annexin V^{+} PI^{+} cell percentages (Q2) were plotted. Bars represent means ± s.e.m.. **, p < 0.05; **, p < 0.01; ***, p < 0.005.* Scale bars: 200 µm.

Supplementary Fig. 2. High *SMPD3* expression inhibits oligodendroglioma cell growth in a suspension system.

A,B. Immunostaining of BT088 (A) and BT054 (B) cells with Sox10 and nSMase2. Merged images of Sox10 (green) and nSMase2 (red) with DAPI as counterstain in blue. **C-G.** To monitor effects of *SMPD3* overexpression in cells in a suspension system, GFP expressing cells (GFP-BT088 cells: Ctrl/Ctrl-GFP; *SMPD3*-GFP-BT088 cells: *SMPD3/ SMPD3*-GFP) were seeded on uncoated plates and growth was monitored by monitoring total area covered by GFP^{+} cells. Representative images of cell growth at day 14, from one independent experiment, is presented (C-F). Mean values of cumulative GFP^{+} area (normalized to day 0) ratio were plotted comparing between days 0 to 14 (G). Bars represent means ± s.e.m..Scale bars: 200 µm.

Supplementary Fig. 3. *SMPD3* knockdown is growth enhancing and recapitulated by GW4869, a pharmacological inhibitor.

A. Western blot for Alix protein of shScr and sh*SMPD3*-A,B,C,D BT088 cell-derived EVs. **B-F.** BT088 cells transduced with shScr and sh*SMPD3*- B,C,D constructs were cultured for 9 days on uncoated plates. Growth was monitored by monitoring total area covered by GFP^{+} cells. Representative images of cell growth at day 9, is presented (B-E). Mean values of total GFP^{+} area normalized to day 0) ratio were plotted comparing between days 0 to 9 (F). **G-K**. BT088 cells

transfected with shScr-GFP and sh*SMPD3*-GFP were cultured for 10 days. Representative images of BT088 shScr-GFP (G) and sh*SMPD3*-GFP (H) tumorspheres after 10 DIV. Quantitation of tumorsphere number (I), tumorsphere size (J), and live cell number (K). **L-O**. BT088 cells transduced with shScr and sh*SMPD3*- B,C,D constructs were cultured for 48 hrs and fixed post a 30 min BrdU pulse. Merged images of fixed cells immunostained with BrdU (red), GFP (green), and DAPI counterstain in blue. **P-T.** BT088 cells treated with DMSO control (Ctrl) and with GW4869 (1 μM) for 14 DIV. Total $CD9^+$ EV particle determination using nanoscale flow cytometry (P,Q). Representative images of Ctrl (R,S) and GW4869 (1 μM) treated cells after 14 DIV. Mean values of total phase object count (relative to day 0) ratio were plotted spanning from day 0 to day 14 (T). **U-X.** BT088 cells treated with Ctrl (U) and 18 μM GW4869 (V) for 5 DIV. Quantitation of the number of tumorspheres (W) and the size of tumorspheres (μm) (X) generated after 5DIV. Bars represent means ± s.e.m.. **, $p < 0.05$; **, $p < 0.01$; ***, $p < 0.005$*; Student's *t* test, and One-way ANOVA when testing more than two groups. Scale bars=200 μm in (B-E); 100 μm in (G,H); 50 μm in (L-O).

Supplementary Fig. 4. Confirming *SMPD3* knockdown of xenografted oligodendroglioma cells.

A,B. BT088 GFP tumor xenograft sections immunostained with nSMase2 (red) and Human Nuclear Antigen (HNA; green), and DAPI as counterstain in blue (A). Region marked in white box in (A) is magnified (4X) and presented in (B). **C.** Western blot for whole HEK cell lysates co-transfected with shScr or *SMPD3* knockdown (KD) construct and *SMPD3* construct. Expression of nSMase2 was assessed for knockdown in *SMPD3* expression. Three biological replicates of each sample set were loaded in varying amounts (5X/1X) to show efficiency of knockdown. **D-G**. Representative images of BT088 cells transfected with shScr (D,D'), and *SMPD3* KD (E-E') cultured for 10DIV (BF, Brightfield). Quantitation of GFP^+ tumorsphere numbers (F) and sphere diameter (μm) (G) after 10 DIV. **H.** hESC cerebral organoid generation protocol. 30day cerebral organoids were co-cultured with BT088 cells (shScr, sh*SMPD3*-B/D) for 7 DIV. Bars represent means ± s.e.m.. Scale bars: 100 μm.

REFERENCES

1. Kickingereder P*, et al.* IDH mutation status is associated with a distinct hypoxia/angiogenesis transcriptome signature which is non-invasively predictable with rCBV imaging in human glioma. *Sci Rep* **5**, 16238 (2015).

2. Huang J, Yu J, Tu L, Huang N, Li H, Luo Y. Isocitrate Dehydrogenase Mutations in Glioma: From Basic Discovery to Therapeutics Development. *Front Oncol* **9**, 506 (2019).

3. Holland EC. Gliomagenesis: genetic alterations and mouse models. *Nat Rev Genet* **2**, 120-129 (2001).

4. Zhu Y, Parada LF. The molecular and genetic basis of neurological tumours. *Nat Rev Cancer* **2**, 616-626 (2002).

5. Messali A, Villacorta R, Hay JW. A review of the economic burden of glioblastoma and the cost effectiveness of pharmacologic treatments. *Pharmacoeconomics* **32**, 1201-1212 (2014).

6. Otani R*, et al.* IDH-mutated astrocytomas with 19q-loss constitute a subgroup that confers better prognosis. *Cancer Sci* **109**, 2327-2335 (2018).

7. Yip S*, et al.* Concurrent CIC mutations, IDH mutations, and 1p/19q loss distinguish oligodendrogliomas from other cancers. *The Journal of pathology* **226**, 7-16 (2012).

8. Bettegowda C*, et al.* Mutations in CIC and FUBP1 contribute to human oligodendroglioma. *Science* **333**, 1453-1455 (2011).

9. Kelly JJ*, et al.* Oligodendroglioma cell lines containing t(1;19)(q10;p10). *Neuro Oncol* **12**, 745-755 (2010).

10. Ahmad ST*, et al.* Capicua regulates neural stem cell proliferation and lineage specification through control of Ets factors. *Nat Commun* **10**, 2000 (2019).

11. Quail DF, Joyce JA. The Microenvironmental Landscape of Brain Tumors. *Cancer Cell* **31**, 326-341 (2017).

12. Colombo M, Raposo G, Thery C. Biogenesis, secretion, and intercellular interactions of exosomes and other extracellular vesicles. *Annu Rev Cell Dev Biol* **30**, 255-289 (2014).

13. Kosaka N, Iguchi H, Yoshioka Y, Takeshita F, Matsuki Y, Ochiya T. Secretory mechanisms and intercellular transfer of microRNAs in living cells. *J Biol Chem* **285**, 17442-17452 (2010).

14. Frohlich D*, et al.* Multifaceted effects of oligodendroglial exosomes on neurons: impact on neuronal firing rate, signal transduction and gene regulation. *Philos Trans R Soc Lond B Biol Sci* **369**, (2014).

15. Guitart K, Loers G, Buck F, Bork U, Schachner M, Kleene R. Improvement of neuronal cell survival by astrocyte-derived exosomes under hypoxic and ischemic conditions depends on prion protein. *Glia* **64**, 896-910 (2016).

16. Kramer-Albers EM, Hill AF. Extracellular vesicles: interneural shuttles of complex messages. *Curr Opin Neurobiol* **39**, 101-107 (2016).

17. Rak J. Extracellular vesicles - biomarkers and effectors of the cellular interactome in cancer. *Frontiers in pharmacology* **4**, 21 (2013).

18. Matarredona ER, Pastor AM. Extracellular Vesicle-Mediated Communication between the Glioblastoma and Its Microenvironment. *Cells* **9**, (2019).

19. Yekula A, Yekula A, Muralidharan K, Kang K, Carter BS, Balaj L. Extracellular Vesicles in Glioblastoma Tumor Microenvironment. *Front Immunol* **10**, 3137 (2019).

20. D'Agostino S, Salamone M, Di Liegro I, Vittorelli ML. Membrane vesicles shed by oligodendroglioma cells induce neuronal apoptosis. *Int J Oncol* **29**, 1075-1085 (2006).

21. Lo Cicero A*, et al.* Oligodendroglioma cells shed microvesicles which contain TRAIL as well as molecular chaperones and induce cell death in astrocytes. *Int J Oncol* **39**, 1353-1357 (2011).

22. Venneti S*, et al.* Evaluation of histone 3 lysine 27 trimethylation (H3K27me3) and enhancer of Zest 2 (EZH2) in pediatric glial and glioneuronal tumors shows decreased H3K27me3 in H3F3A K27M mutant glioblastomas. *Brain Pathol* **23**, 558-564 (2013).

23. Ligon KL*, et al.* The oligodendroglial lineage marker OLIG2 is universally expressed in diffuse gliomas. *J Neuropathol Exp Neurol* **63**, 499-509 (2004).

24. Dennis CV, Suh LS, Rodriguez ML, Kril JJ, Sutherland GT. Human adult neurogenesis across the ages: An immunohistochemical study. *Neuropathol Appl Neurobiol* **42**, 621-638 (2016).

25. Pitt JM, Marabelle A, Eggermont A, Soria JC, Kroemer G, Zitvogel L. Targeting the tumor microenvironment: removing obstruction to anticancer immune responses and immunotherapy. *Ann Oncol* **27**, 1482-1492 (2016).

26. Coles-Takabe BL*, et al.* Don't look: growing clonal versus nonclonal neural stem cell colonies. *Stem Cells* **26**, 2938-2944 (2008).

27. Cornelissen M, Philippe J, De Sitter S, De Ridder L. Annexin V expression in apoptotic peripheral blood lymphocytes: an electron microscopic evaluation. *Apoptosis* **7**, 41-47 (2002).

28. Jeppesen DK*, et al.* Reassessment of Exosome Composition. *Cell* **177**, 428-445 e418 (2019).

29. Padda RS*, et al.* Nanoscale flow cytometry to distinguish subpopulations of prostate extracellular vesicles in patient plasma. *Prostate* **79**, 592-603 (2019).

30. Beit-Yannai E, Tabak S, Stamer WD. Physical exosome:exosome interactions. *J Cell Mol Med* **22**, 2001-2006 (2018).

31. Otto GP, Nichols BJ. The roles of flotillin microdomains--endocytosis and beyond. *J Cell Sci* **124**, 3933-3940 (2011).

32. Brennan K*, et al.* A comparison of methods for the isolation and separation of extracellular vesicles from protein and lipid particles in human serum. *Sci Rep* **10**, 1039 (2020).

33. Zomer A*, et al.* In Vivo imaging reveals extracellular vesicle-mediated phenocopying of metastatic behavior. *Cell* **161**, 1046-1057 (2015).

34. Choi DS, Kim DK, Kim YK, Gho YS. Proteomics of extracellular vesicles: Exosomes and ectosomes. *Mass Spectrom Rev* **34**, 474-490 (2015).

35. Shabnam B*, et al.* Sorcin a Potential Molecular Target for Cancer Therapy. *Transl Oncol* **11**, 1379-1389 (2018).

36. Beiko J*, et al.* IDH1 mutant malignant astrocytomas are more amenable to surgical resection and have a survival benefit associated with maximal surgical resection. *Neuro Oncol* **16**, 81-91 (2014).

37. Silvestre JS*, et al.* Lactadherin promotes VEGF-dependent neovascularization. *Nat Med* **11**, 499-506 (2005).

38. Chen HM, Tsai CH, Hung WC. Foretinib inhibits angiogenesis, lymphangiogenesis and tumor growth of pancreatic cancer in vivo by decreasing VEGFR-2/3 and TIE-2 signaling. *Oncotarget* **6**, 14940-14952 (2015).

39. Hofmann K, Tomiuk S, Wolff G, Stoffel W. Cloning and characterization of the mammalian brain-specific, Mg2+-dependent neutral sphingomyelinase. *Proc Natl Acad Sci U S A* **97**, 5895-5900 (2000).

40. Engelhard HH, Stelea A, Mundt A. Oligodendroglioma and anaplastic oligodendroglioma: clinical features, treatment, and prognosis. *Surg Neurol* **60**, 443-456 (2003).

41. Iwadate Y*, et al.* Eighty percent survival rate at 15 years for 1p/19q co-deleted oligodendroglioma treated with upfront chemotherapy irrespective of tumor grade. *J Neurooncol* **141**, 205-211 (2019).

42. Bannykh SI, Stolt CC, Kim J, Perry A, Wegner M. Oligodendroglial-specific transcriptional factor SOX10 is ubiquitously expressed in human gliomas. *J Neurooncol* **76**, 115-127 (2006).

43. Kapustin AN*, et al.* Vascular smooth muscle cell calcification is mediated by regulated exosome secretion. *Circ Res* **116**, 1312-1323 (2015).

44. Trajkovic K*, et al.* Ceramide triggers budding of exosome vesicles into multivesicular endosomes. *Science* **319**, 1244-1247 (2008).

45. Catalano M, O'Driscoll L. Inhibiting extracellular vesicles formation and release: a review of EV inhibitors. *J Extracell Vesicles* **9**, 1703244 (2020).

46. Hardee ME, Zagzag D. Mechanisms of glioma-associated neovascularization. *Am J Pathol* **181**, 1126-1141 (2012).

47. Colodner KJ, Montana RA, Anthony DC, Folkerth RD, De Girolami U, Feany MB. Proliferative potential of human astrocytes. *J Neuropathol Exp Neurol* **64**, 163-169 (2005).

48. Wesseling P, van den Bent M, Perry A. Oligodendroglioma: pathology, molecular mechanisms and markers. *Acta Neuropathol* **129**, 809-827 (2015).

49. Lancaster MA, Knoblich JA. Generation of cerebral organoids from human pluripotent stem cells. *Nat Protoc* **9**, 2329-2340 (2014).

50. Kelava I, Lancaster MA. Dishing out mini-brains: Current progress and future prospects in brain organoid research. *Dev Biol* **420**, 199-209 (2016).

51. Linkous A*, et al.* Modeling Patient-Derived Glioblastoma with Cerebral Organoids. *Cell Rep* **26**, 3203-3211 e3205 (2019).

52. Qian X, Jacob F, Song MM, Nguyen HN, Song H, Ming GL. Generation of human brain region-specific organoids using a miniaturized spinning bioreactor. *Nat Protoc* **13**, 565-580 (2018).

53. Neskovic NM, Rebel G, Harth S, Mandel P. Biosynthesis of galactocerebrosides and glucocerebrosides in glial cell lines. *J Neurochem* **37**, 1363-1370 (1981).

54. Wu BX, Clarke CJ, Hannun YA. Mammalian neutral sphingomyelinases: regulation and roles in cell signaling responses. *Neuromolecular Med* **12**, 320-330 (2010).

55. Peng CH, Huang CN, Hsu SP, Wang CJ. Penta-acetyl geniposide induce apoptosis in C6 glioma cells by modulating the activation of neutral sphingomyelinase-induced p75 nerve growth factor receptor and protein kinase Cdelta pathway. *Mol Pharmacol* **70**, 997-1004 (2006).

56. Kim WJ*, et al.* Mutations in the neutral sphingomyelinase gene SMPD3 implicate the ceramide pathway in human leukemias. *Blood* **111**, 4716-4722 (2008).

57. Ostrowski M*, et al.* Rab27a and Rab27b control different steps of the exosome secretion pathway. *Nat Cell Biol* **12**, 19-30; sup pp 11-13 (2010).

58. Zhang L*, et al.* Microenvironment-induced PTEN loss by exosomal microRNA primes brain metastasis outgrowth. *Nature* **527**, 100-104 (2015).

59. Gao X*, et al.* Gliomas Interact with Non-glioma Brain Cells via Extracellular Vesicles. *Cell Rep* **30**, 2489-2500 e2485 (2020).

60. Podbielska M*, et al.* Cytokine-induced release of ceramide-enriched exosomes as a mediator of cell death signaling in an oligodendroglioma cell line. *J Lipid Res* **57**, 2028-2039 (2016).

61. Choi D, Montermini L, Kim DK, Meehan B, Roth FP, Rak J. The Impact of Oncogenic EGFRvIII on the Proteome of Extracellular Vesicles Released from Glioblastoma Cells. *Mol Cell Proteomics* **17**, 1948-1964 (2018).

62. Al-Nedawi K*, et al.* Intercellular transfer of the oncogenic receptor EGFRvIII by microvesicles derived from tumour cells. *Nat Cell Biol* **10**, 619-624 (2008).

63. Treps L, Perret R, Edmond S, Ricard D, Gavard J. Glioblastoma stem-like cells secrete the pro-angiogenic VEGF-A factor in extracellular vesicles. *J Extracell Vesicles* **6**, 1359479 (2017).

64. Xu C, Wu X, Zhu J. VEGF promotes proliferation of human glioblastoma multiforme stem-like cells through VEGF receptor 2. *ScientificWorldJournal* **2013**, 417413 (2013).

65. Shapiro B, Tocci P, Haase G, Gavert N, Ben-Ze'ev A. Clusterin, a gene enriched in intestinal stem cells, is required for L1-mediated colon cancer metastasis. *Oncotarget* **6**, 34389-34401 (2015).

66. Datta A*, et al.* High-throughput screening identified selective inhibitors of exosome biogenesis and secretion: A drug repurposing strategy for advanced cancer. *Sci Rep* **8**, 8161 (2018).

67. Wang J, Bonacquisti EE, Brown AD, Nguyen J. Boosting the Biogenesis and Secretion of Mesenchymal Stem Cell-Derived Exosomes. *Cells* **9**, (2020).

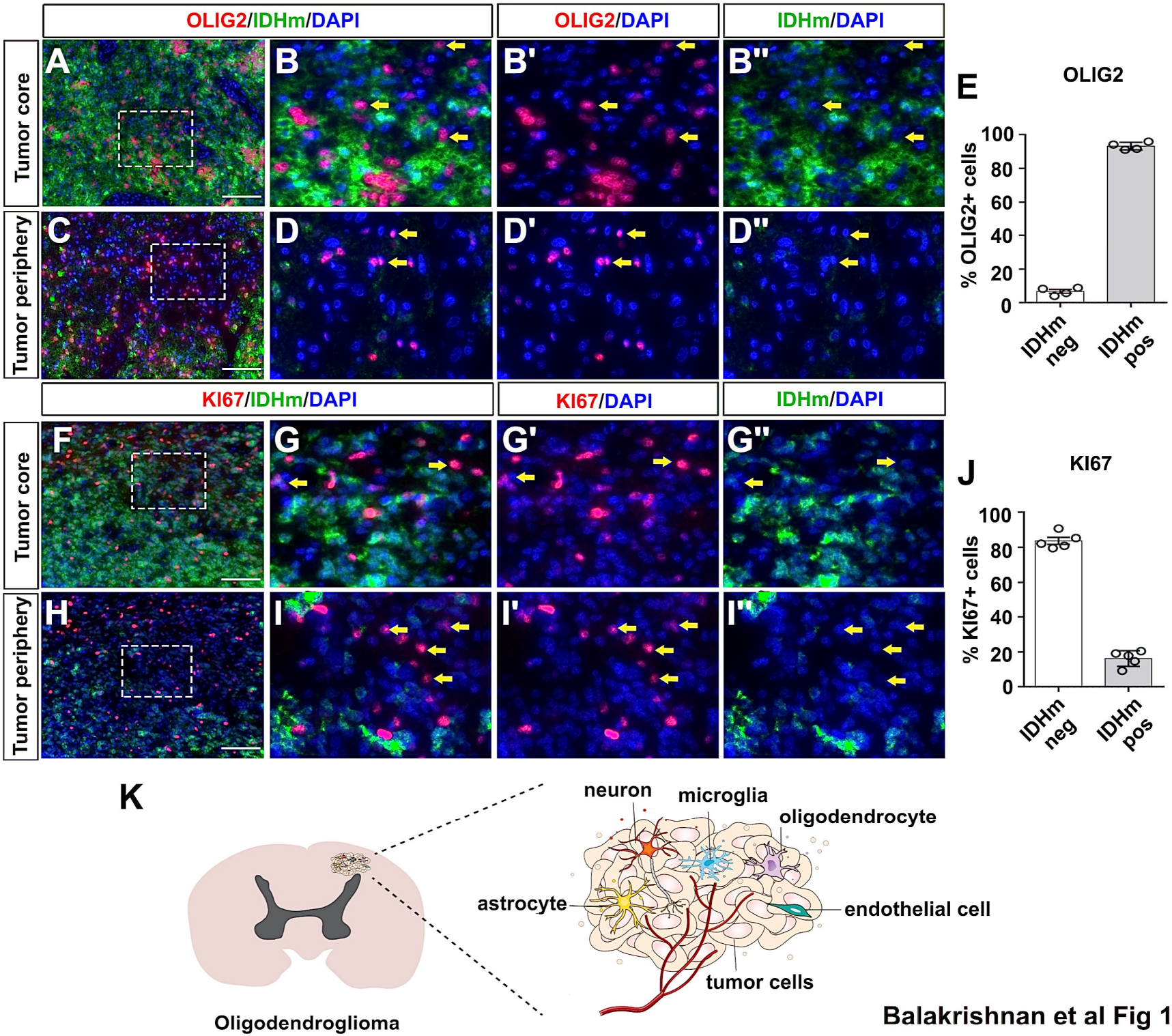

Balakrishnan et al Fig 1

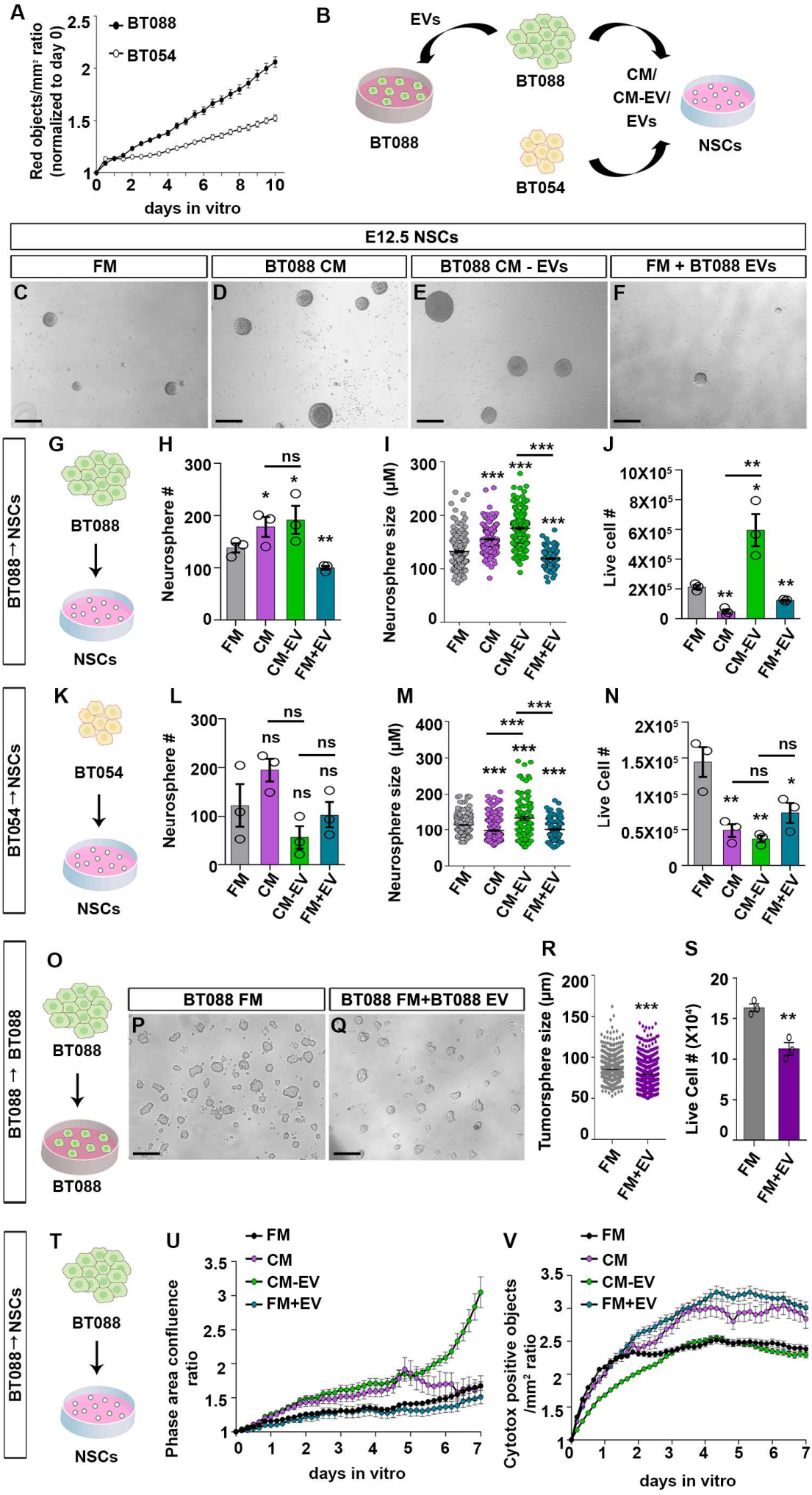

Balakrishnan et al. Figure 2

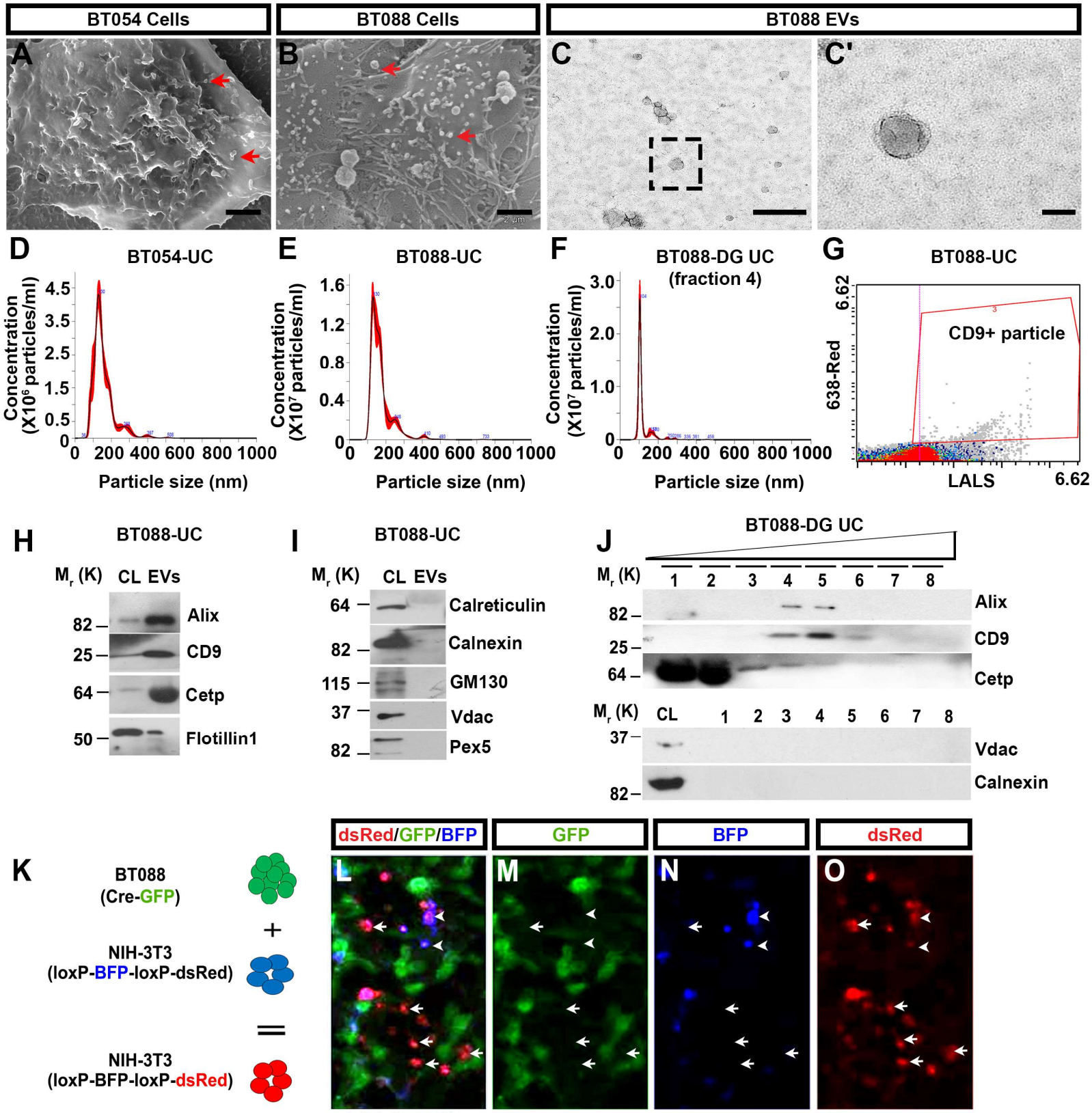

Balakrishnan et al. Figure 3

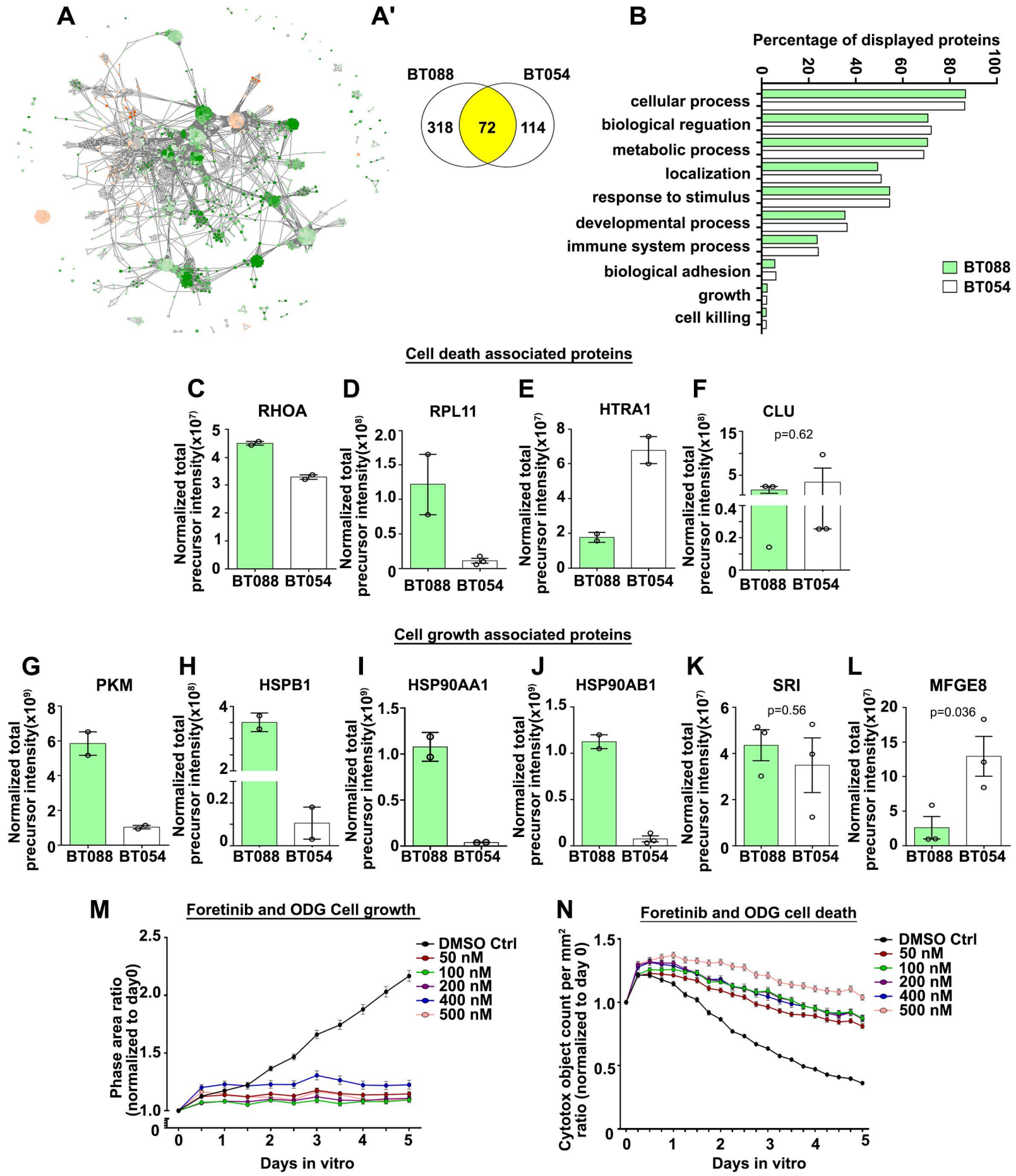

Balakrishnan et al. Figure 4

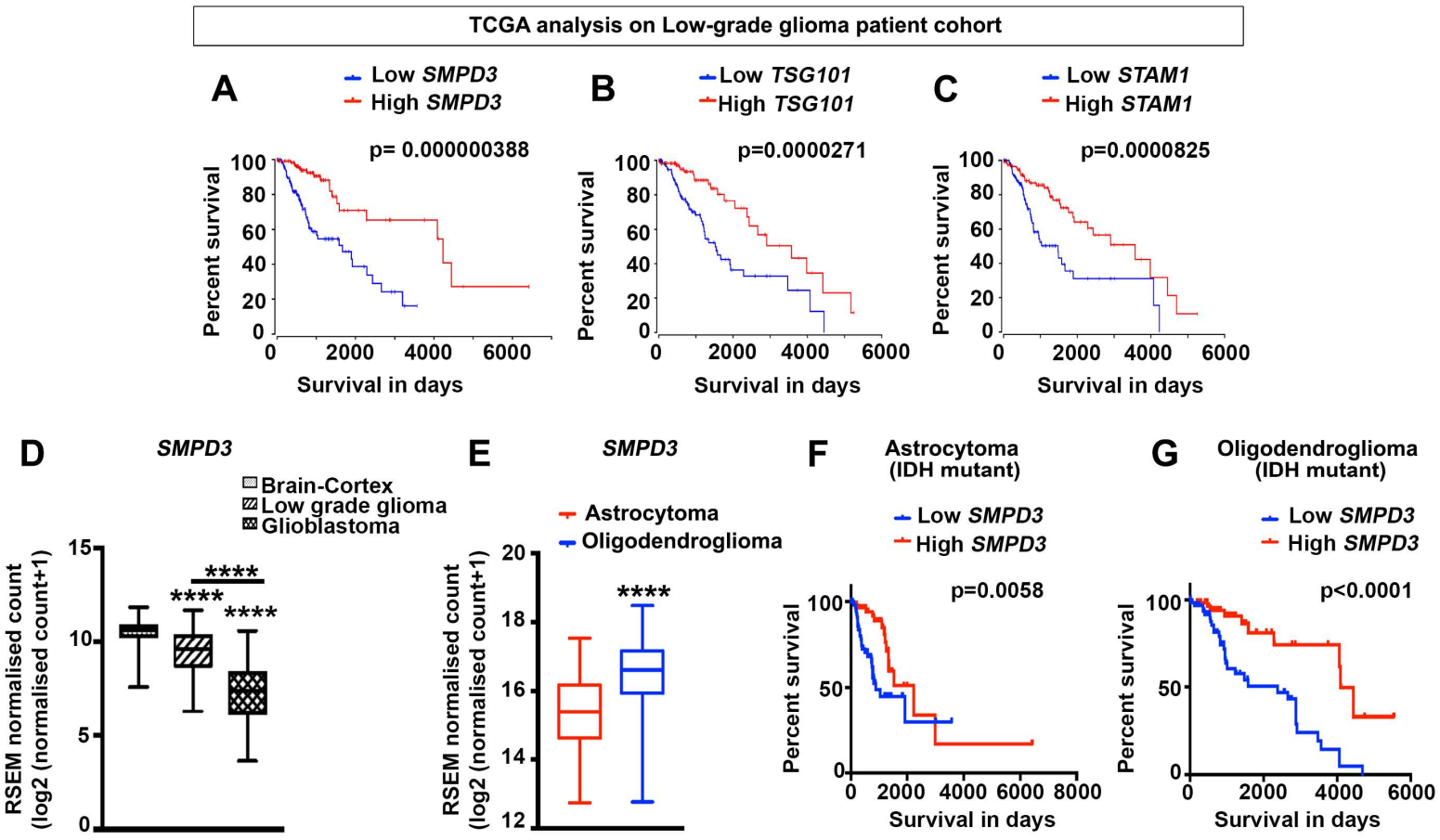

Balakrishnan et al. Figure 5

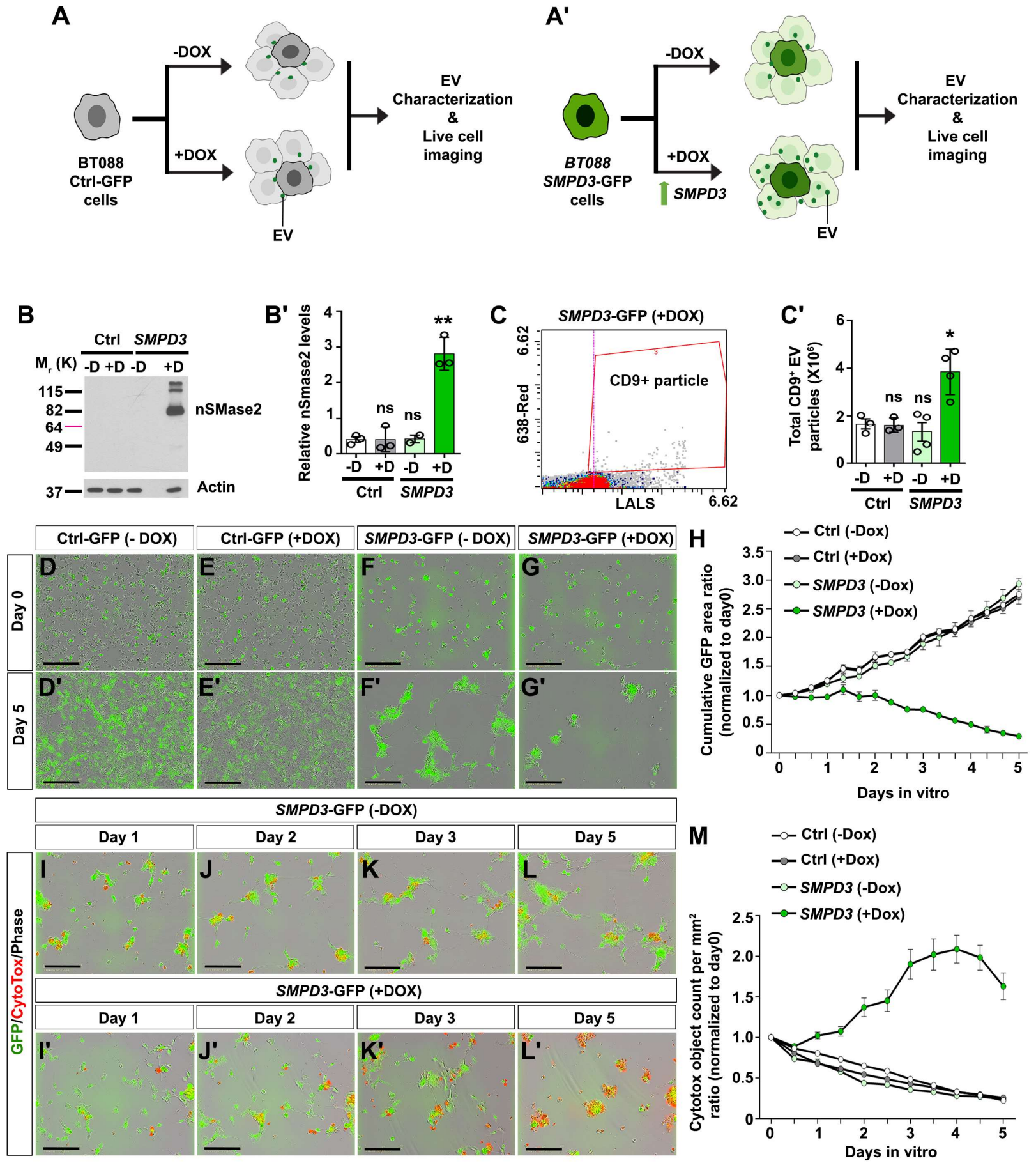

Balakrishnan et al. Figure 6

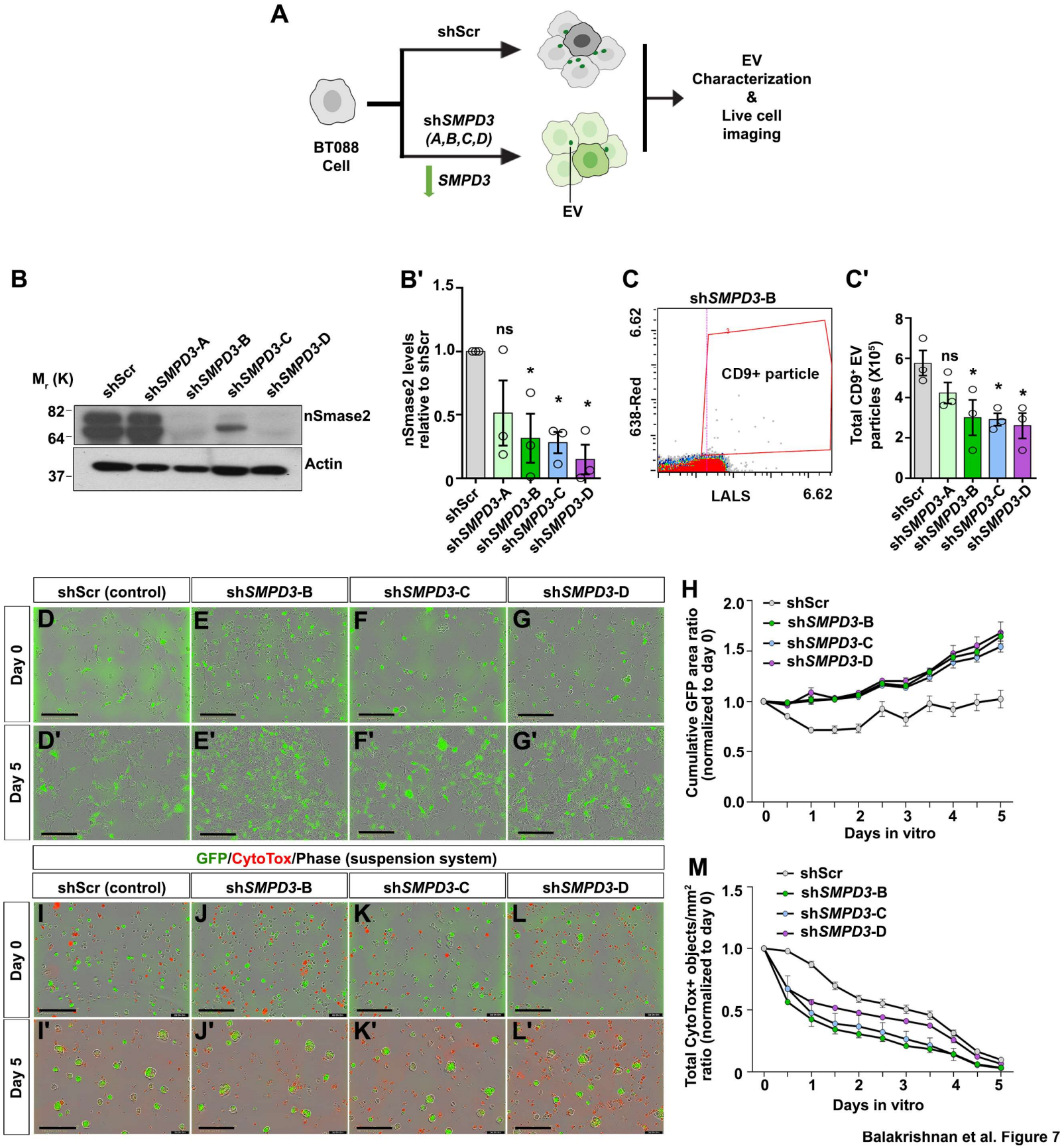

Balakrishnan et al. Figure 7

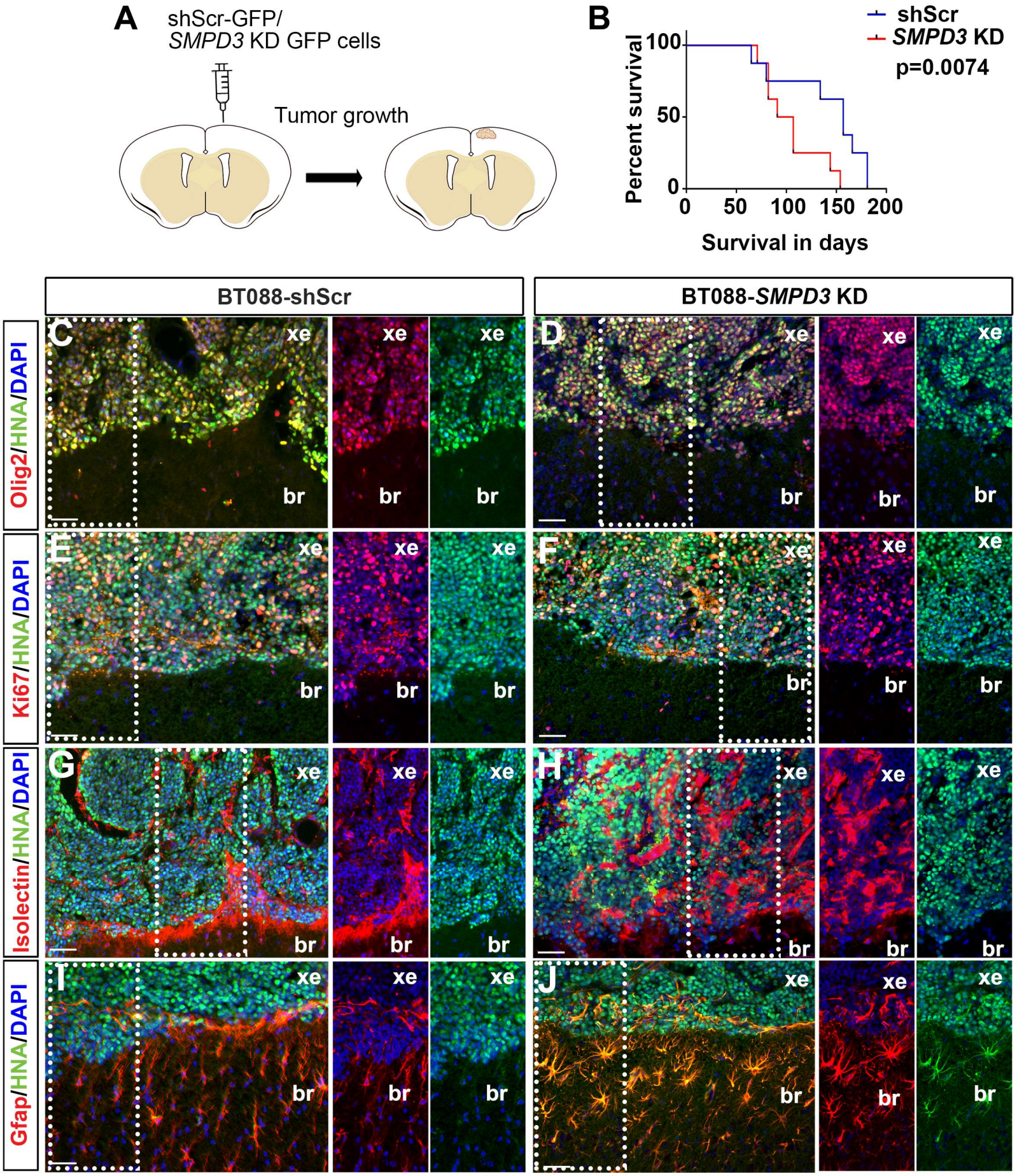

Balakrishnan et al. Figure 8

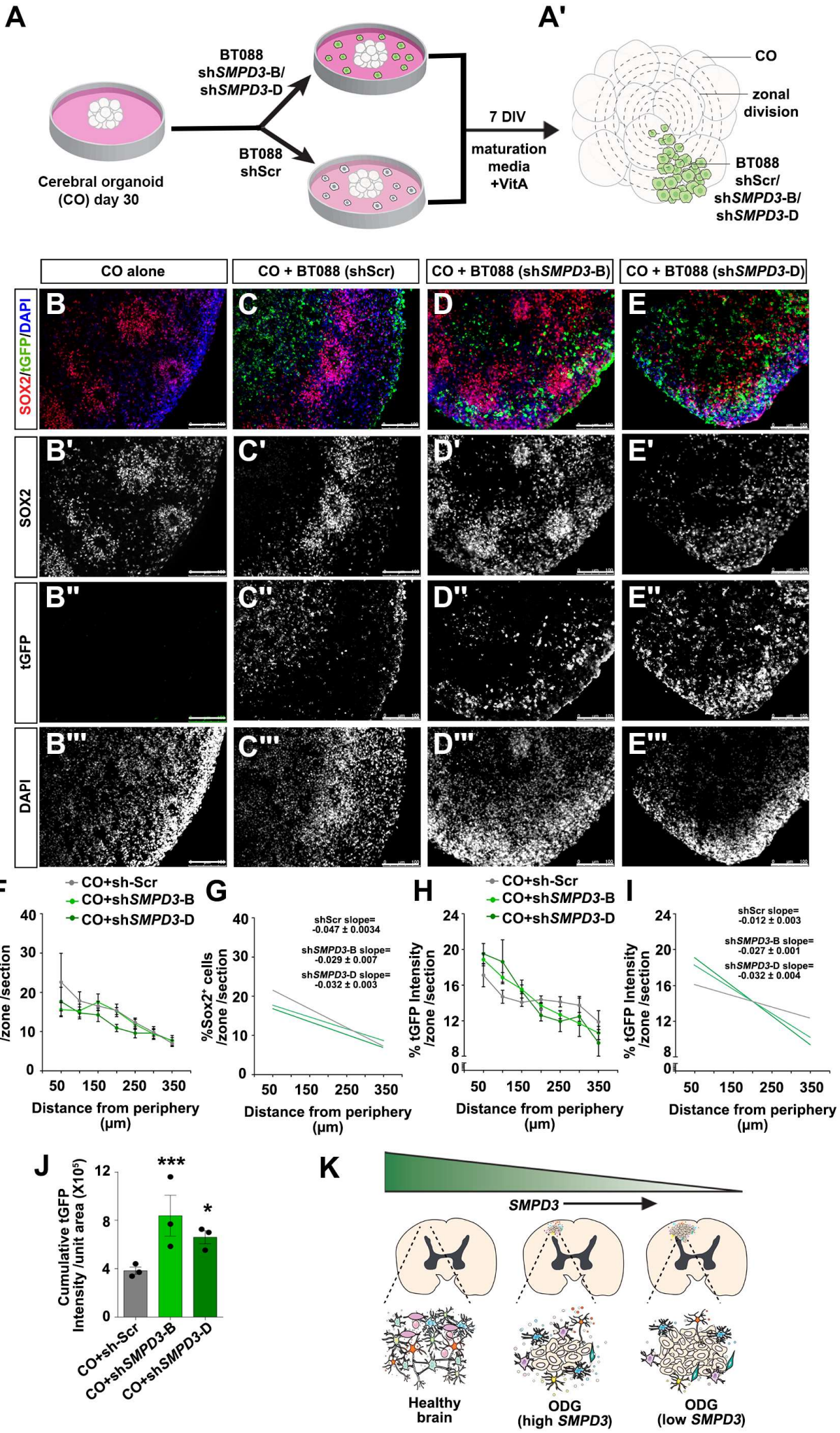

Balakrishnan et al. Figure 9

Sample ID	Gender	Age	WHO classification	WHO grade	IDH1/2 status
SM-2296	F	47	Oligodendroglioma, IDH-mutant and 1p/19q-codeleted	II	IDH1 mut
SM-2624	M	31	Anaplastic oligodendroglioma, IDH-mutant and 1p/19q-codeleted	III	IDH1 mut
SM-2857	M	45	Anaplastic oligodendroglioma, IDH-mutant and 1p/19q-codeleted	III	IDH1 mut
SM-3201	F	61	Anaplastic oligodendroglioma, IDH-mutant and 1p/19q-codeleted	III	IDH1 mut
SM-3435	M	45	Anaplastic oligodendroglioma, IDH-mutant and 1p/19q-codeleted	III	IDH2 mut

Table 1